

Performances of Platinum and nitrogen Dual-Doped Ordered Mesoporous Carbon as Sulfur Host for Li-S Battery

Deyu Qu¹, Rong Li¹, Xinxin Zhu¹, Kai Chen², Yafei Shen², Dan Liu¹, Zhongyuan Ma¹, Shichao Zhang¹, Zhizhong Xie^{1,*}, Junsheng Li¹, Jiaheng Lei¹, Haolin Tang^{3,*}

¹Department of Chemistry, School of Chemistry, Chemical Engineering and Life Science, Wuhan University of Technology, 122 Luoshi Road, Wuhan 430070, Hubei, P.R. China

²Wuhan Jingce Electronic Technology Co., Ltd., Wuhan 430070, China

³State Key Laboratory of Advanced Technology for Material Synthesis and Processing, Wuhan University of Technology, 122 Luoshi Road, Wuhan, 430070 Hubei, PR China

*E-mail: thln@whut.edu.cn, zhizhong_xie@163.com

Received: 7 July 2018 / Accepted: 31 August 2018 / Published: 1 October 2018

Two types of *Resorcinol-Formaldehyde* (RF) resin based ordered mesoporous carbon materials were used as sulfur host in lithium sulfur battery system. The effects of carbon material structure, morphology, surface area, pore volume, sulfur loading, electrolyte/sulfur ratio and metallic Pt nanoparticle decoration impact on the adsorption of polysulfides and battery performance are studied. Results show that carbon material carrying rod-like morphology and hexagonal meso-structure can have high sulfur loading due to its high specific surface area and large pore volume. While the one with polyhedral particles and ordered cubic meso-structure exhibits good cyclic stability and good capacity retention due to its good adsorption of polysulfides upon its cage-like pores. After in-situ decorating of Pt nanoparticles, the performance of cyclic stability as well as capacity retention significantly improved and better rate performance is also gained because of the chemisorption of polysulfides and electro-catalytic activity upon Pt.

Keywords: Ordered mesoporous carbon; lithium sulfur battery; polysulfides chemisorption; shuttle effect; electrocatalytic activity of Pt

1. INTRODUCTION

With merit of high energy of 2500 Wh kg⁻¹, the lithium-sulfur battery now becomes a promising energy storage system over traditional lithium ion batteries and attract a lot of attentions. This device couples the lithium electrode, carrying 3840 mAh g⁻¹ capacity, with the element sulfur electrode, which provides over 1670 mAh g⁻¹ capacity along with its nature abundant, low cost and environment benignity [1-4]. The Li-S battery can deliver an average cell voltage of 2.2 V based on the reversible redox reaction

between sulfur and lithium sulfide (Li_2S) along with a series of polysulfides (Li_2S_x , $4 < x < 8$) as intermediate products [5, 6]. Those polysulfides are highly soluble in organic electrolyte solvent and caused the so called “shuttle effect” which resulted in the consuming of the active material, quick capacity fading, poor cyclic stability and so on. Furthermore, the insolubility of sulfur and Li_2S , which carry insulating nature, may also result in the low utility of active material. Those are the two major challenges in commercialize the Li-S battery in addition with other hurdles like high volume expansion, lithium metal degradation, and so on.

To cope with those drawbacks, many studies focus on the using of carbon materials, especially the micro-mesoporous carbon, as sulfur host [7-9]. Carbon material can not only provide a high conductivity and buffer medium to improve conductivity of active material and endure the strain caused by the volume change during the charge/discharge process, but also trap the soluble polysulfides within the carbon matrix through physic-interaction [10, 11]. Moreover, the meso-porous structure can also provide the lithium ions diffusion and transfer channels to improve the electrochemical performance [12-14]. Doping carbon materials with heteroatom, such as N, O, F, transition metals and/or transition metal oxides, precious metals to supply the chemisorption sites for polysulfide, is another strategy to enhance the performances of Li-S battery [15-16]. In this study, two RF based carbon materials with ordered mesoporous structure are synthesized and applied as sulfur host in Li-S battery. The impacts of morphology, meso-structure, surface area, pore volume, sulfur loading as well as sulfur/electrolyte ratio upon the electrochemical performance of Li-S battery are evaluated. Furthermore, metallic Pt nanoparticles are also in-situ decorated onto mesoporous carbon materials to study the chemisorption of polysulfide and electrochemical catalytic effects on Li-S system.

2. EXPERIMENTAL SECTION

2.1 Chemicals

Triblock poly(ethylene oxide)-b-poly(propylene oxide)-b-poly(ethylene oxide) copolymers Pluronic F127 ($\text{EO}_{106}\text{PO}_{70}\text{EO}_{106}$, $M_n = 12600$), K_2PtCl_4 and sulfur (99.95%) were purchased from Sigma-Aldrich Corp. Other chemicals were purchased from Sinopharm Chemical Reagent Corp. All chemicals were used as received without further purification.

2.2 Synthesis of Cubic RF-1 and Hexagonal RF-2

We have followed the same procedures described in our previous paper [17]. (1) Cubic RF-1. In a typical procedure, 11.0 g of resorcinol (R), 7.0 g of HMT, 20.0 g of Pluronic F127, 500 mL of deionized water and 20.0 mL of aqueous ammonia (28 wt %) were mixed in random sequence. After stirring at room temperature for 1 h, the resultant dark green solution was further stirred in a water-bath under reflux condenser at 80 °C. Green precipitation was observed after about 20 min. After continuously stirring for another 24 h, the black solid products were collected by sedimentation separation, filtration, washed with water and air-dried at room temperature. Finally, the as-made composite was thermally

treated at 900 °C for 3 h, with a heating rate of 1 °C min⁻¹ under a nitrogen atmosphere, to obtain the RF-1. (2) Hexagonal RF-2. About 11.0 g of resorcinol, 7.0 g of HMT, 20.0 g of Pluronic F127, 4.0 g of TMB, 520 mL of deionized water and 20.0 mL of aqueous ammonia (28 wt %) were mixed. After stirring at room temperature for 2 h, the solution was further stirred at 80 °C for 24 h. The products were collected and calcined as in the above procedure, to obtain RF-2.

2.3 Synthesis of RF-1-A and RF-2-A

The post-synthesis KOH activation was performed by mixing typical sample RF-1 (RF-2) with a KOH ethanol solution (KOH/carbonmass ratio was 5.0) followed by an evaporation step at 60 °C under stirring in a nitrogen atmosphere. Then, the dry mixture was heated up to 750 °C min⁻¹ with a ramping rate of 1.5 °C min⁻¹ in a highpurity argon atmosphere (>99.999%) and annealed for 3 h. The activated sample was thoroughly washed with 1 M HCl solution and deionized water, and eventually dried at 120 °C for 12 h. The obtained carbon was denoted as RF-1-A (RF-2-A).

2.4 Synthesis of RF-1-Pt and RF-2-Pt

In a typical experiment, 3.6 g of the as-synthesized polymer product (dried at 120 °C overnight) was redispersed in 100 mL of 1.2 M HCl solution containing and 0.2 g of K₂PtCl₄, and stirred at room temperature for 8 h. Then, the product was collected by filtration, washed three times with deionized water, and dried at 50 °C under vacuum for 8 h. The final RF-1-Pt and RF-2-Pt was obtained after pyrolysis under H₂/Ar (5%/95%) atmosphere. The pyrolysis procedure was as follows: the sample was heated to 350 °C and 900 °C for 3 h with a rate of 1 °C min⁻¹.

2.5 Synthesis of RF-1-Pt-A and RF-2-Pt-A

The synthesis conditions for RF-1-Pt-A and RF-2-Pt-A were the same as that for RF-1-A and Hexagonal RF-2-A.

2.6 Preparation of RF-1-A, RF-2-A, RF-1-Pt-A and RF-2-Pt-A composites

The RF-1-A and sulfur (Aladdin, 99.95%) were well mixed in different weight ratio (based on the volume of sulfur and end product Li₂S) and then the mixture was sealed in a Teflon pot and heated in 155 °C for 24 h. After cooling to room temperature, the S/RF-1-A composite was obtained. The S/RF-2-A, S/RF-1-Pt-A and S/RF-2-Pt-A composites were synthesized by the same method.

2.7 Electrochemical Measurements

To make the cathode, 75 wt % carbon/sulfur composite material, 15 wt % Super-P conductive carbon, 10 wt % LA133 were mixed in deionized water to form a homogeneous slurry, and then the

slurry as spread onto a carbon-coated Al foil and dried at 50 °C for 12 h. Subsequently, the electrode was cut into round with a diameter of 15 mm with the active material loading of about $2.0 \pm 0.2 \text{ mg cm}^{-2}$. The 2032-type coin cells were assembled in a glovebox filled with Ar with Celgard 2400 membrane as separator and Li metal as anode. The electrolyte was composed of 1 M lithium bis (trifluoromethanesulfonyl) imide (LiTFSI) in a mixture of 1,3-dioxolane (DOL) and dimethoxymethane (DME) (v/v = 1:1) added with 0.4 M LiNO₃. Galvanostatic tests were performed in the potential range of 1.5-2.8 V vs Li/Li⁺ at 25 °C using a LAND CT2001A battery-testing instrument. The cyclic voltammetry (CV) were recorded on electrochemical station (CHI660E) at a scanning rate of 0.2 mV S⁻¹ in the voltage range of 1.5-2.8 V. The electrochemical impedance spectroscopy (EIS) tests were carried out at open circuit voltage and the fully charged states after 100 cycles in the frequency ranges of 100k Hz and 100 mHz with a perturbation amplitude of 5 mV.

2.8 Characterization

The small-angle X-ray diffraction (XRD) measurements were performed on a Bruker D8 Advance diffractometer with a Cu K α radiation ($\lambda = 1.5406 \text{ \AA}$) operating at 40 kV, 40 mA. Transmission electron microscopy (TEM) images were recorded on a JEM 2100F electron microscope operating at 200 kV. Scanning electron microscopy (SEM) observation was carried out using a Hitachi S-4800 microscope. X-ray photoelectron spectroscopy (XPS) measurements were performed by a Thermo VG Multilab 2000 spectrometer with a monochromatic Al K α X-ray source. Nitrogen sorption isotherms were obtained at 77 K with an ASAP 2400 (Micromeritics, US). The carbon/sulfur composite material were degassed at 50 °C for 4-8 h under vacuum. The pore size distributions (PSDs) were calculated from adsorption data of isotherms using the Tarazona's non-local density functional theory (NLDFT) method and the density functional theory (DFT) method, respectively.

3. RESULTS AND DISCUSSION

3.1 Results and Discussion of RF-1-A and RF-2-A

3.1.1 Morphology and Structure Characterization

Highly ordered mesoporous carbon materials RF-1, RF-2 as the matrix material are not only improve the conductivity of the active material, but also have a strong adsorption effect on the intermediate product long-chain polysulfides during the discharge process [17]. In order to achieve higher sulfur content and better inhibition effect on the shuttle effect, the RF-1, RF-2, as examples, were treated by well-established KOH chemical activation to obtain higher surface area and pore volume carbon materials RF-1-A, RF-2-A. The X-ray diffraction (XRD) pattern of RF-1 (Fig. 1a) shows three well-resolved diffraction peaks at $2\theta = 0.5-2.5^\circ$ can be indexed as (110), (200), and (211) reflections of the body-centered cubic $\text{Im}\bar{3}\text{m}$ symmetry, indicating that a highly ordered cubic mesoscopic structure. Fig. 1b presents the XRD patterns of RF-2 with three well-resolved diffraction peaks can be indexed as

(10), (11), and (20) reflections of 2-D hexagonal mesostructure with long-range order (space group: $p6m$) [18]. Importantly, the XRD pattern of RF-1-A and RF-2-A still exhibit three sharp XRD peaks assigned to $Im\bar{3}m$ symmetry and $p6m$ symmetry respectively in spite of the peak intensity significantly drops, suggesting good framework stability of the material.

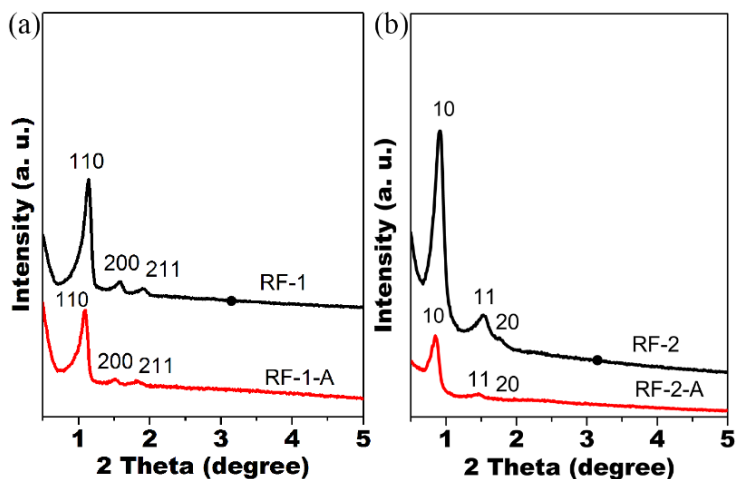


Figure 1. Small-angle XRD patterns of (a) RF-1, RF-1-A and (b) RF-2, RF-2-A.

Although lithium-sulfur battery has a high theoretical capacity, both sulfur and intermediate products are electrical insulators. In order to improve electronic conductivity of electrode, various approaches have been assumed to add a large amount of conductive agent or reduce the thickness of coating, which lead to two lows including low sulfur content and low sulfur loading so that advantage of energy density is offset [19-25]. Nevertheless, excess sulfur blocks carbon channels, meantime, aggravating shuttle effect and eventually fast capacity fading. In consequence, it is vital to balance ratio for C/S composite cathode. Here, we design two different sulfur loading for RF-1-A and RF-2-A based on the volume of sulfur and the end product Li_2S (Table 1).

Table 1. Theoretical calculation of sulfur content

| | Sulfur | Li_2S |
|------------------------|--------|---------|
| RF-1-A-50S, RF-1-A-60S | 58.2% | 43.5% |
| RF-2-A-60S, RF-2-A-70S | 67.5% | 53.4% |

$$m_s = V_t \times m_c \times \rho \times \frac{32}{46}$$

m_s : quality of sulfur, V_t : pore volume of carbon material, $cm^3 g^{-1}$, ρ : $1.66 g cm^{-3}(Li_2S)$, m_c : quality of carbon material.

In this case, the a-b, e-f of Fig. 2 show SEM images of RF-1, RF-1-A, RF-2, and RF-2-A, respectively. The RF-1 grains are about 5-10 μm in size with irregular polyhedral particles which can be seen clearly growth patterns on the surface. For RF-2, rod-like domains with the size of 500 nm in length and 200 nm in diameter aggregating along the long axis can be observed. From the particles of RF-1-A and RF-2-A, we can see the surface of the particles are only rough without destroying the structure of the material, which is consistent with the XRD peaks intensity change.

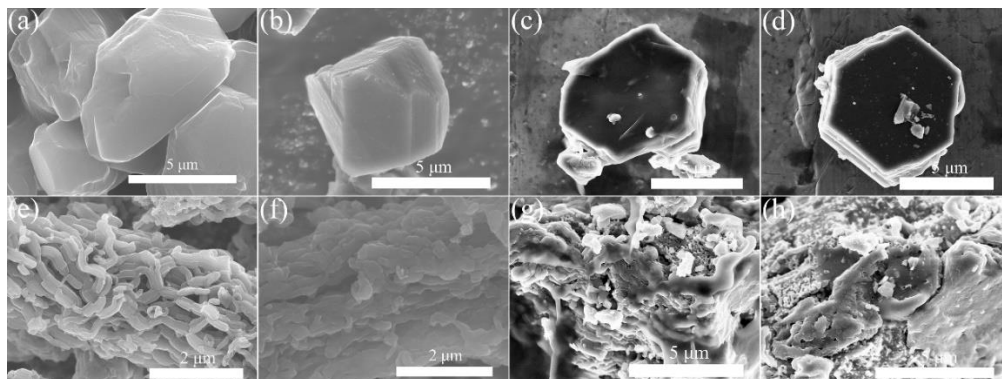


Figure 2. SEM images of (a) RF-1, (b) RF-1-A, (c) RF-1-A-50S, (d) RF-1-A-60S, (e) RF-2, (f) RF-2-A, (g) RF-2-A-60S and (h) RF-2-A-70S.

SEM images of four different C/S composites are displayed in parts of c-d, g-h of Fig. 2. There are no visible large bulk sulfur particles on the surface of RF-1-A-50S and RF-2-A-60S, which suggests that sulfur is uniformly distributed throughout the carbon frameworks. Whereas the aggregates of sulfur particles are clearly observed on the other two C/S composites with higher sulfur loading especially for RF-2-A-70S. This can be corroborated by the XRD patterns (Fig. 3).

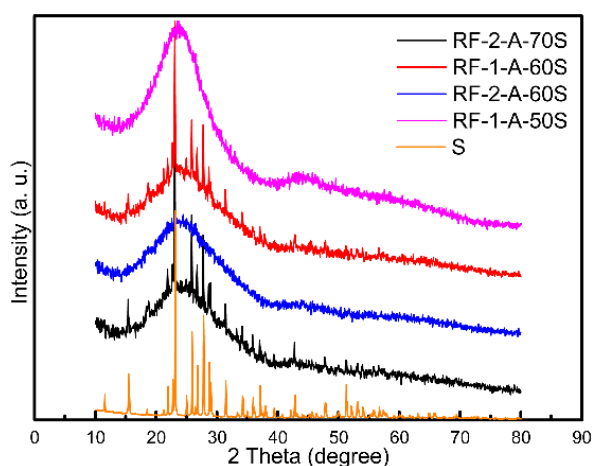


Figure 3. XRD patterns of pure S, RF-1-A-50S , RF-1-A-60S, RF-2-A-60S, and RF-2-A-70S.

There are only two C/S composites show well-resolved diffraction peaks indexed to Fddd orthorhombic structure reflections of elemental sulfur, which indicate the formation of nano-crystalline

domain after melting and condensificiation during the process. In contrast, RF-1-A-50S and RF-2-A-60S composite exhibit reduced peak intensity for sulfur, which match well with expected design results.

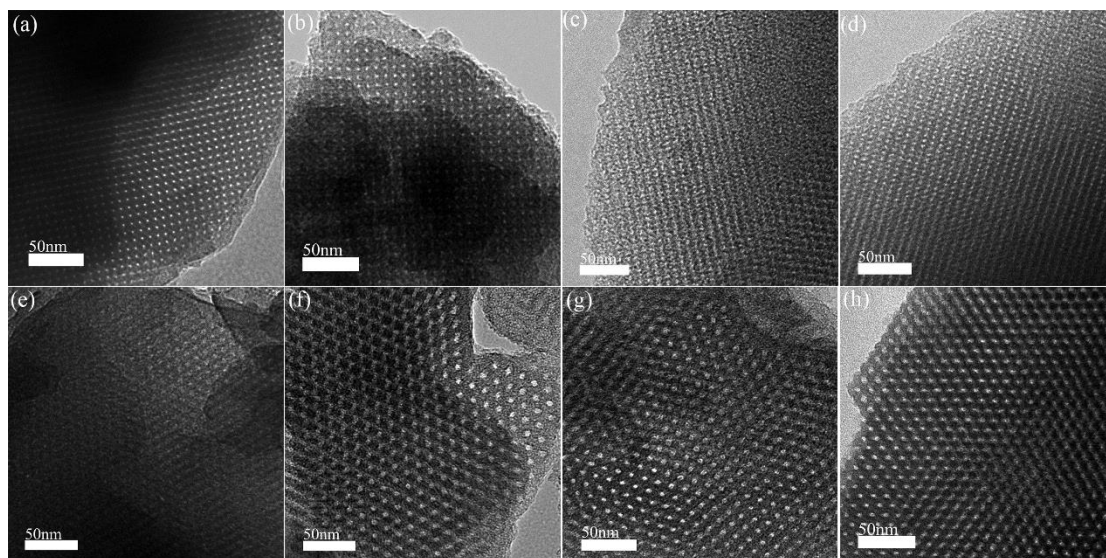


Figure 4. TEM images of (a) RF-1, (b) RF-1-A, (c) RF-1-A-50S, (d) RF-1-A-60S, (e) RF-2, (f) RF-2-A, (g) RF-2-A-60S and (h) RF-2-A-70S.

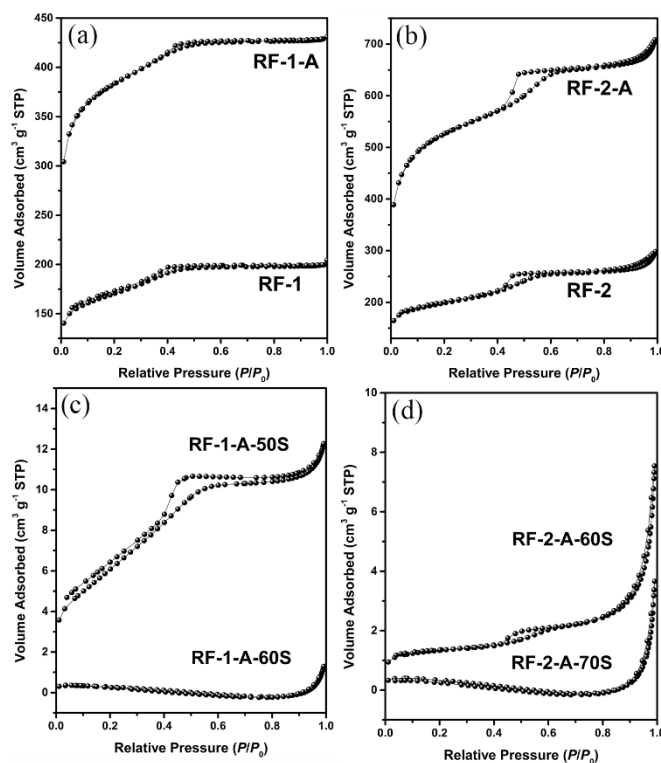


Figure 5. Nitrogen sorption isotherms of different carbon hosts before and after sulfur impregnation: (a) RF-1, RF-1-A, (b) RF-2, RF-2-A, (c) RF-1-A-50S, RF-1-A-60S, and (d) RF-2-A-60S, RF-2-A-70S.

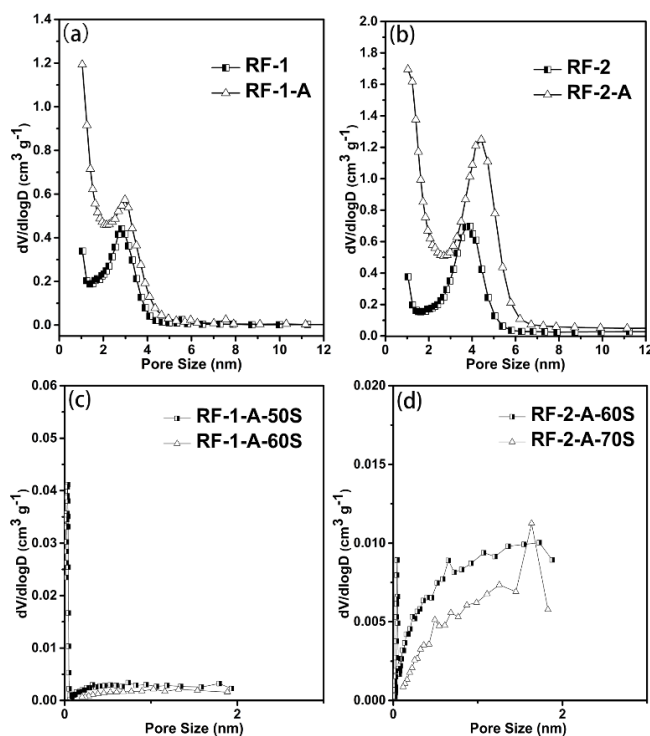


Figure 6. PSD curves of (a) RF-1, RF-1-A, (b) RF-2, RF-2-A, (c) RF-1-A-50S, RF-1-A-60S, and (d) RF-2-A-60S, RF-2-A-70S.

Table 2. Structural parameters of carbon samples

| Sample | S_{BET}^a ($\text{m}^2 \text{g}^{-1}$) | V_t^b ($\text{cm}^3 \text{g}^{-1}$) | S_{mi}^c ($\text{m}^2 \text{g}^{-1}$) | V_{mi}^d ($\text{cm}^3 \text{g}^{-1}$) |
|------------|--|--|---|--|
| RF-1-A | 1344 | 0.667 | 1031 | 0.459 |
| RF-2-A | 1857 | 0.991 | 1325 | 0.582 |
| RF-1 | 580 | 0.32 | 333 | 0.16 |
| RF-2 | 662 | 0.46 | 416 | 0.20 |
| RF-1-A-50S | 22.11 | 0.02 | 0 | 0 |
| RF-1-A-60S | 0.91 | 0.002 | 0 | 0 |
| RF-2-A-60S | 4.6 | 0.01 | 0 | 0 |
| RF-2-A-70S | 1.1 | 0.001 | 0 | 0 |

^a S_{BET} : BET specific surface area; ^b V_t : total volume; ^c S_{mi} : micropore surface area, was calculated from t -plot method; ^d V_{mi} : micropore volume, was calculated from t -plot method.

As seen in Fig. 4, the TEM images of RF-1 exhibit large well-ordered domains, further demonstrating the ordered cubic $\text{Im}\bar{3}m$ mesostructure. Honeycomb-like TEM images reveal that RF-2 possesses a high-quality hexagonal mesostructure which consist of pure 2-D hexagonal mesophase. Apart from the increase of pore size, the mesoscopic structure of RF-1-A and RF-2-A have not undergone obvious change after KOH chemical activation, in good agreement with the XRD data. All the TEM images (Fig. 4c, 4d, 4g, 4h) become somewhat blurred after the sulfur loading because some of the sulfur crystallizes poorly during the rapid cooling which prove sulfur change from solid to liquid into the pores of the carbon material during the heating process.

The nitrogen sorption isotherms are presented in Fig. 5. Both of the RF-1 and RF-1-A are representative Type-IV curve with clear capillary condensation steps at $P/P_0=0.4-0.6$ and Type-H2 hysteresis loops, suggesting cage-type pores with small entrances [26], which is conducive to suppress the dissolution and diffusion of polysulfides. RF-2 and RF-2-A also display Type-IV isotherms with Type-H1 hysteresis loops, indicating uniform mesopore distributions. These long-range-ordered channels not only shorten the transmission path of ions and electrons, but also accelerate reaction kinetics and improve the utilization rate of sulfur. Surface area and pore volume of different carbon and C/S composites are summarized in Table 2. As observed, surface area and pore volume are dramatically increased after treating by well-established KOH chemical activation. For instance, RF-2-A has more than nearly triple in surface area, the pore volume increase from $0.46 \text{ cm}^3 \text{ g}^{-1}$ to $0.991 \text{ cm}^3 \text{ g}^{-1}$. The primary mesopore diameter of RF-1-A and RF-2-A from PSD curve (Fig. 6) are about 3.0 nm and 4.4 nm respectively, slightly larger than that for RF-1 (2.8 nm) and RF-2 (3.9 nm). This is owing to the formation of new micropores in mesopore walls by carbon etching. All the efforts are aimed at reducing the shuttle effect and volume expansion. As expected, surface area and pore volume of RF-1-A and RF-2-A decline sharply after sulfur impregnation, demonstrating sulfur is filled with the inner pore space of carbon. This is also confirmed by the disappearance of mesopores in the PSD curve, which is the same as the change in surface area and pore volume. However, when C/S ratio is below the theoretical sulfur loading of 58.2% and 67.5% respectively, it can be ensured that some of the interspaces still exist in the carbon material, as corroborated by the hysteresis in isotherms of RF-1-A-50S and RF-2-A-60S find obviously in Fig. 6c, 6d. This is conducive to the infiltration of electrolyte into the interior during the same standing time. These evidences demonstrate surface area and pore volume played a decisive role in accommodate most sulfur inside the carbon matrix.

Besides the structure of the carbon material, the oxygen-containing functional groups may also be beneficial to anchoring sulfur and suppressing the diffusion of polysulfides, thereby improving cycle performance[27]. To determine the extent of the binding between the carbon and sulfur nanocrystals, X-ray photoelectron spectroscopy (XPS) measurements further investigated. After KOH activation, both RF-1-A and RF-2-A still retain some oxygen containing functional groups, as shown in Fig. 7a, 7b. The C 1s spectrum of RF-1-A can be divided into four kinds of peaks, corresponding to C-C bond (284.5 eV), C=N bond (285.3 eV), C-O bond (286.4 eV), and C=O bond (288.4 eV), respectively. It is worth noting that the peak of C=O groups decrease and become narrower, which reveals C=O groups are removed and converted to C-O-S bonds during melting-diffusion process (Fig. 7c, 7e, 7g, 7i). Meanwhile, in the S 2p spectra of RF-1-A-50S and RF-1-A-60S, the $2p_{3/2}$ (163.6 and 164.8 eV) and $2p_{1/2}$ (164.3 and 165.5 eV) spin orbit levels are assigned to S-S bond and S-O species [28, 29], respectively.

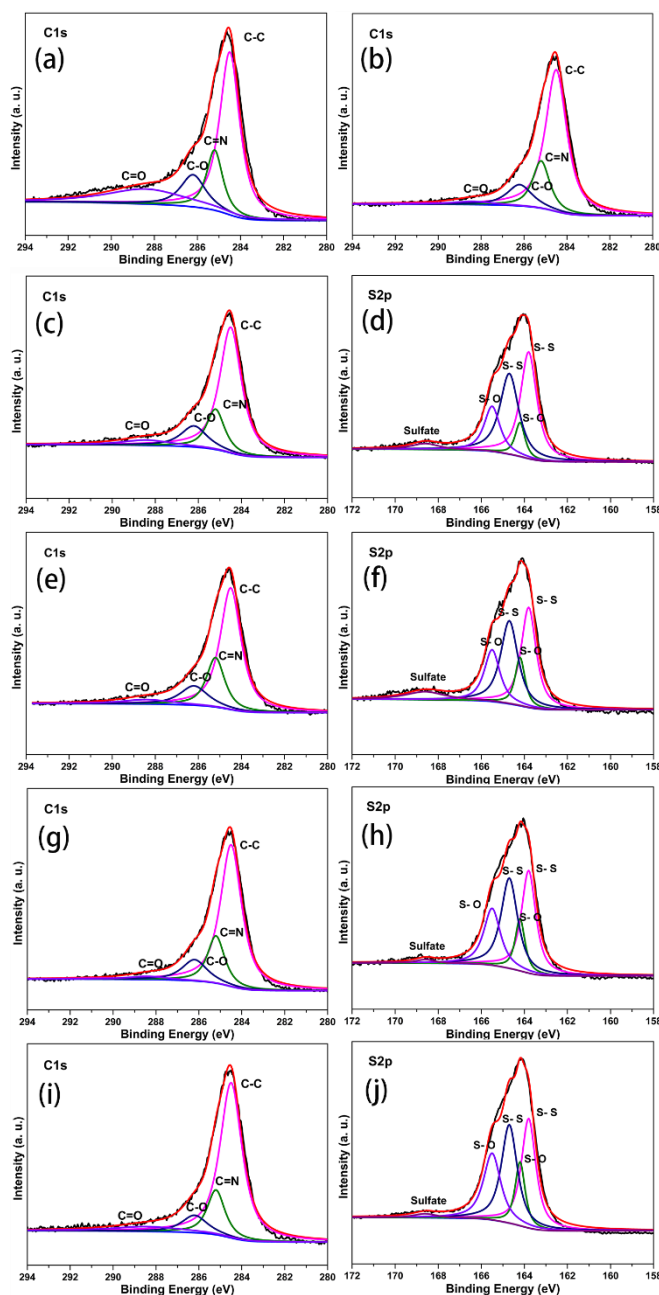


Figure 7. High-resolution C 1s and S 2p spectra of (a) RF-1-A, (b) RF-2-A, (c, d) RF-1-A-50S, (e, f) RF-1-A-60S, (g, h) RF-2-A-60S and (i, j) RF-2-A-70S.

The other small peak at 168.6 eV can be attributed to the sulfate species formed by the oxidation of sulfur in air. All the results imply the sulfur nanocrystals maintain intimate contact with carbon through S-O bonding. The results of RF-2-A are also found to be similar with those of RF-1-A. The presence of S-O species prevents the loss of active materials. In addition, nitrogen atoms are also present in the carbon material, which has proven to immobilize corresponding polysulfides during the discharge/charge process [30]. There are a total of four peaks with a binding energy of 398.3 eV, 400.2 eV, 401.1 eV, and 402.9 eV can be detected, which correspond to pyridinic-N (N-6), pyrrolic-N (N-5), quaternary-N (N-Q) and oxidized pyridine-N (N-X) [31], respectively (Fig. 8a-f). It should be noted that,

due to the KOH activation at high temperatures, the loss of a large amount of N atoms in the carbon material is expected.

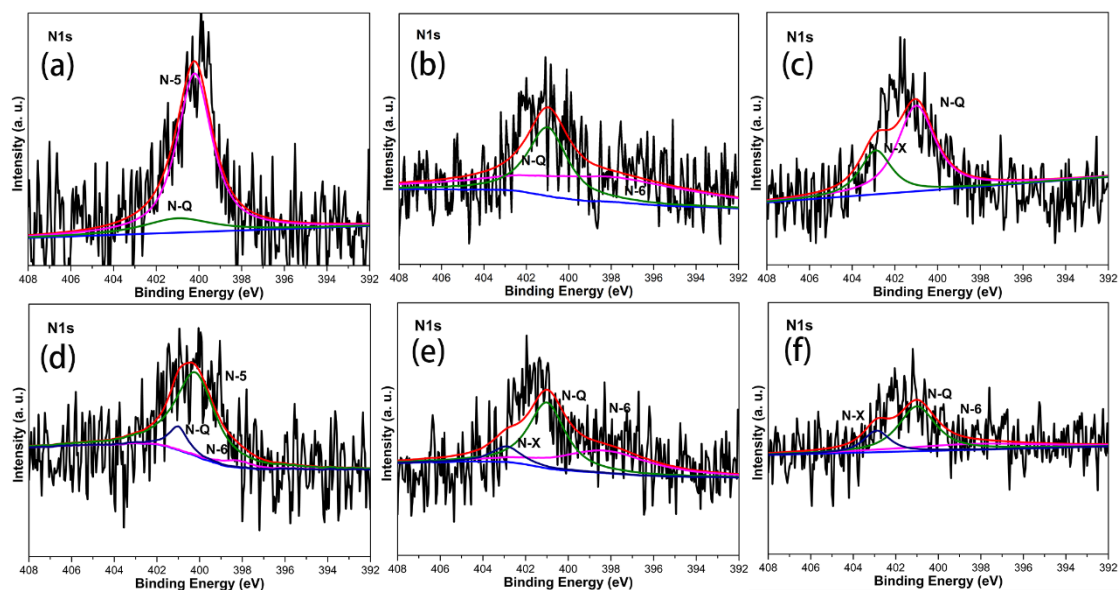


Figure 8. High-resolution N 1s spectra of (a) RF-1-A, (b) RF-1-A-50S, (c) RF-1-A-60S, (d) RF-2-A, (e) RF-2-A-60S and (f) RF-2-A-70S.

3.1.2 Discussion of different E/S ratios

The dissolution and diffusion of polysulfides have a close relationship with the amount of electrolyte which is one of the important parameters affect the capacity and cycling performance of Li-S battery [32]. The optimized ratio between electrolyte and solid sulfur change with sulfur content and carbon matrix materials. Hence, optimizing E/S ratio of two kinds of mesoporous carbon materials in different sulfur content is first investigated. Fig. 9 compares the galvanostatic charge/discharge profiles and cyclic performances of RF-2-A-70S cells with three different E/S ratios at current densities of 0.1 C (1 C = 1675 mA g⁻¹_{sulfur}) in the voltage range of 1.5-2.8 V (vs. Li⁺/Li). All the discharge profiles with two typical plateaus are exhibited at ca. 2.3 V and ca. 2.1 V respectively in accordance with previous literatures [33-35]. It can be seen that as the E/S ratio was increased from 15 μL mg⁻¹ to 30 μL mg⁻¹, the initial discharge capacities of 772.5, 861.1, and 872.3 mAh g⁻¹ (based on sulfur) are synchronously increased, while the initial Coulombic efficiencies of 93.3%, 89.7% and 85.8% express contrary trend. When the measurements go on, the cell with E/S ratio of 15 μL mg⁻¹ demonstrate highest capacity retention of 56.25% than other two E/S ratio. The more dissolution and faster diffusion rate of polysulfides caused by excess amount of electrolyte result in shuttle reactions and lithium anode corrosion occurring more quickly. The second plateau is a liquid-solid two-phase reaction including a series of complicated disproportionations and plays a decisive role in discharge capacity. Therefore, the sufficient contact between polysulfides-containing electrolyte and carbon matrix is particularly important. It is worth to note a reasonably high sulfur loading density (2.0 ± 0.2 mg cm⁻²) was employed in all cells. From comparison the charge/discharge profiles of the three cells, increasing polarization can

be observed during the first discharge process due to highly concentrated electrolyte with high viscosity and poor wetting capability on the electrode. However, the subsequent discharge process returned to normal because of re-dissolution and re-deposition process of sulfur on the electrode. Obviously, the optimized E/S ratio is fixed at a value of $15 \mu\text{L mg}^{-1}$.

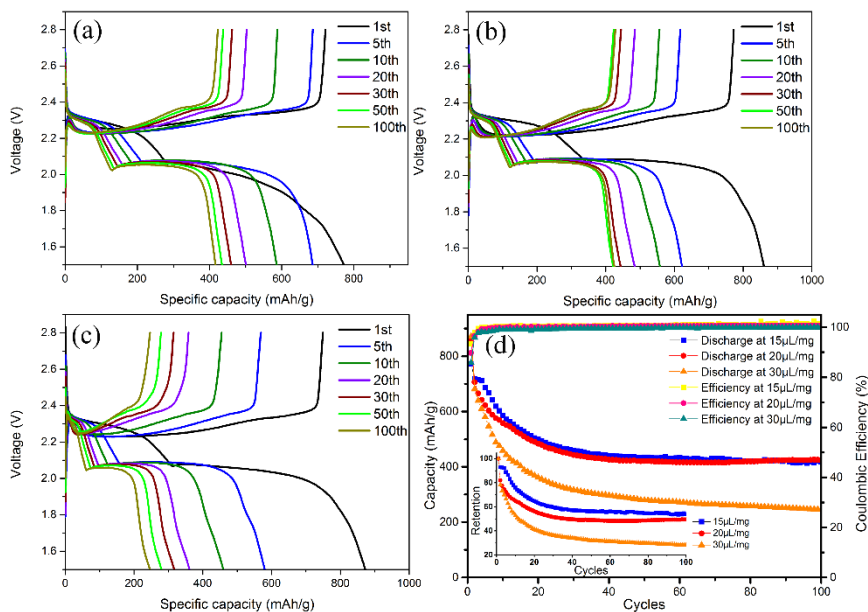


Figure 9. Charge/discharge profiles and cyclic performances of RF-2-A-70S electrodes with three different E/S ratios at 0.1 C in a voltage range of 1.5-2.8 V: (a) $15 \mu\text{L mg}^{-1}$, (b) $20 \mu\text{L mg}^{-1}$ and (c) $30 \mu\text{L mg}^{-1}$.

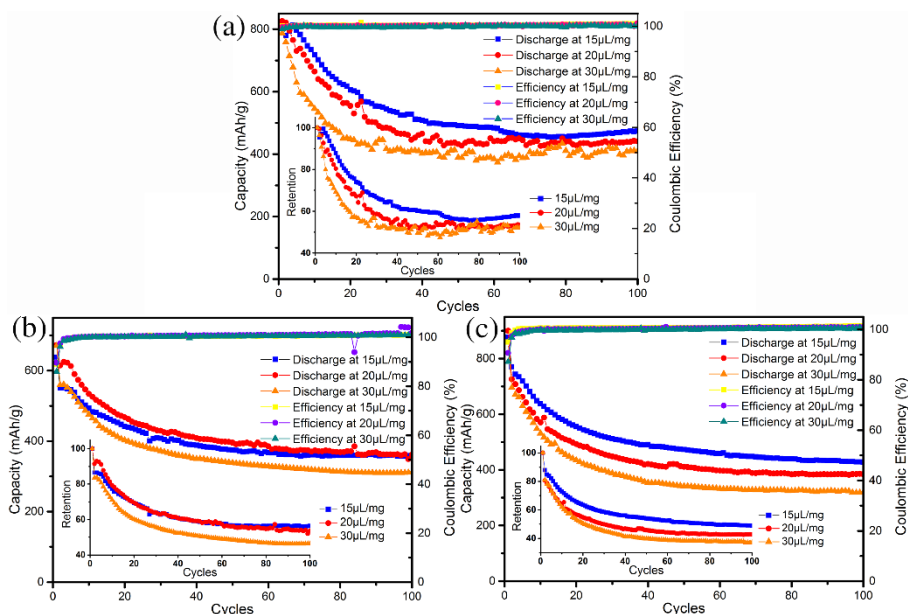


Figure 10. The cyclic performances of (a) RF-1-A-50S, (b) RF-1-A-60S and (c) RF-2-A-60S electrodes with three different E/S ratios at 0.1 C in a voltage range of 1.5-2.8 V (inset : retention).

The cyclic performances of other C/S composites with three different E/S ratios are showed in Fig. 10. The results are strikingly similar to that of RF-2-A-70S. Interestingly, the cyclic performance as

well as the capacity retention of RF-1-A-60S are found to overlap (Fig. 10b) with E/S ratio of $15 \mu\text{L mg}^{-1}$ and $20 \mu\text{L mg}^{-1}$, as the sulfur loading overtop the theoretical loading value. The reason for this phenomenon is that excessive sulfur loading counteracts the influence of the loss of active material due to the polysulfides dissolution into electrolyte and diffusion into the cell's dead corners. After initial decreasing, the trend of Coulombic efficiency almost keep constant at 100% up to 100 cycles for four C/S composites, which is benefited from addition of LiNO_3 [25, 36-39] and strong physical adsorption of mesoporous. The subsequent electrochemical tests are assembled using the E/S ratio of $15 \mu\text{L mg}^{-1}$.

3.1.3 Electrochemical Performance

To accurately understand the impact of carbon-sulfur ratio and morphology of carbon on electrochemical performance, the RF-1-A-50S, RF-1-A-60S, RF-2-A-60S, and RF-2-A-70S electrode were made by the same process and applied in Li-S battery. The cycle voltammograms (CVs) (Fig. 11) of these four electrodes measured at 0.1 mV s^{-1} show similar electrochemical features and match well with previous studies [40-42]. Two peaks appeared at ca. 2.27 and ca. 2.00 V can be assigned to the reduction from the solid sulfur (S_8) to long-chain polysulfidess (Li_2S_x , $4 < x < 8$) and then to short-chain one (such as Li_2S_2 , Li_2S), respectively. A single oxidation peak is observed at ca. 2.50 V, corresponding to the transformations from lower order lithium sulfides to solid sulfur. There are no obvious variations in peak positions occur the subsequence cycles after 1st cycle, suggesting good reversibility and stability of the electrode. Whereas, two problems with the reduction peaks in the CVs of RF-1-A-60S, RF-2-A-60S, and RF-2-A-70S electrodes are worth mentioning. First, the 1st cycle of the second reduction peak is flat rather than sharp, which proves that sulfur is gradually reduced during the first discharge. High sulfur content and high sulfur loading hinder the infiltration of electrolyte, leading to increase the polarization, and a continuous negative shift in the reduction potential. Therefore, the CV curves show such a discharge potential hysteresis. Second, the first reduction peak current is larger than the second one. Unlike other rechargeable lithium batteries, the electrolyte component and viscosity change with depth of discharge, which affected the nucleation and growth of $\text{Li}_2\text{S}_2/\text{Li}_2\text{S}$. The 2.27 V peak is related to the chemical process control, so all five cycles tend to coincide. Nevertheless, the 2.00 V peak is dominated by the diffusion process. There is a competitive electrochemical reactions from S_4^{2-} to S_3^{2-} and from S_3^{2-} to $\text{Li}_2\text{S}_2/\text{Li}_2\text{S}$ [43]. Because of high sulfur loading and physical adsorption within mesopores, the concentrations of S_3^{2-} near the carbon skeleton increase rapidly but diffuse slowly towards the electrolyte. Thereby, the reaction from S_3^{2-} to $\text{Li}_2\text{S}_2/\text{Li}_2\text{S}$ occur in advance. The generated insoluble $\text{Li}_2\text{S}_2/\text{Li}_2\text{S}$ not only block the pore, but also result in poor conductivity and serious polarization. S_4^{2-} species are not completely reduced until the end of discharge, giving rise to low peak current.

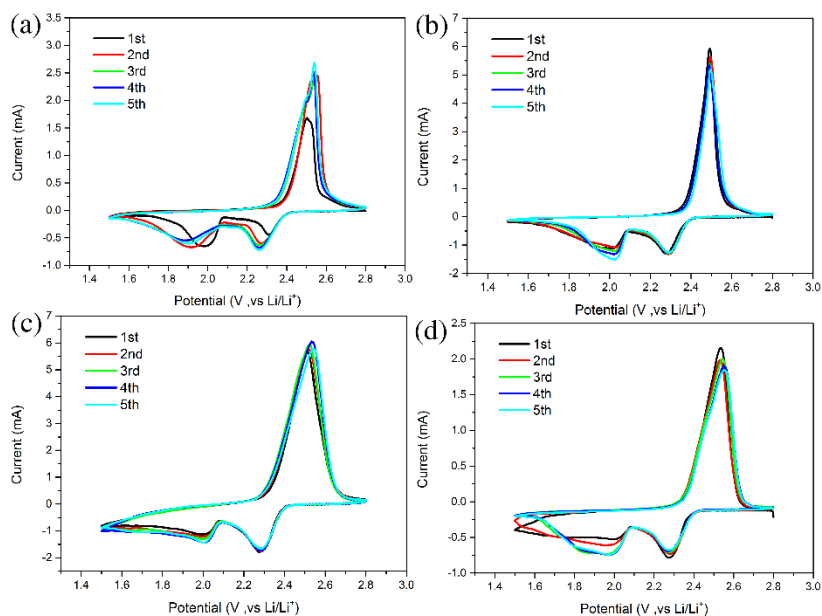


Figure 11. Cycle voltammetry of (a) RF-1-A-50S, (b) RF-1-A-60S, (c) RF-2-A-60S and (d) RF-2-A-70S electrodes at scan rate of 0.1 mV s^{-1} between 1.5 to 3.0 V.

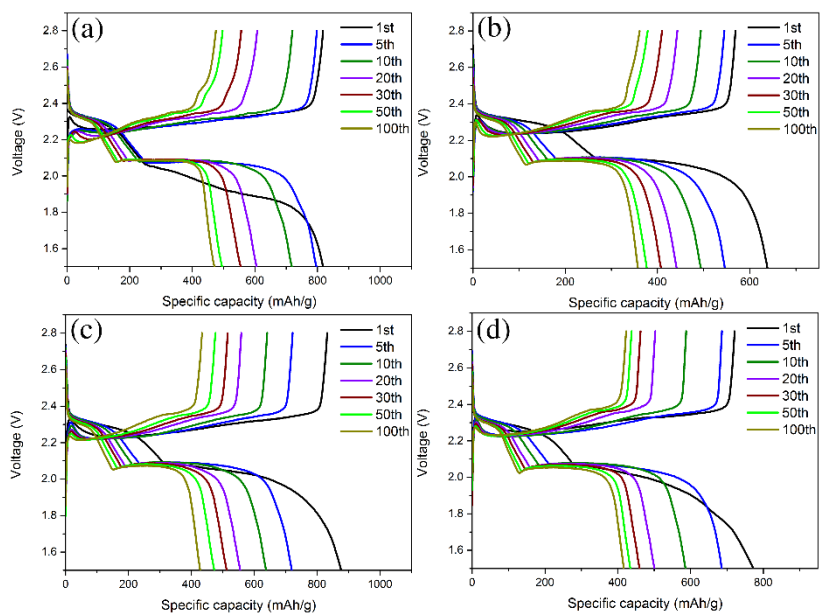


Figure 12. Charge/discharge profiles of (a) RF-1-A-50S, (b) RF-1-A-60S, (c) RF-2-A-60S and (d) RF-2-A-70S electrodes under the current density of 0.1 C in a voltage of 1.5-2.8 V.

Fig. 12 shows the charge-discharge measurements of these four C/S cathodes. When tested at a rate of 0.1 C, all the discharge profiles have two lithiation voltage plateaus which agree with the CV curves. The RF-1-A-50S and RF-1-A-60S electrodes deliver initial discharge capacities of 817.6 and 638.6 mAh g^{-1} with initial Coulombic efficiencies of 99.9% and 89%, respectively. After 100 cycles, the discharge capacities degrade rapidly to 473.5 and 357.8 mAh g^{-1} , which are 57.9% and 56% of that in the first cycle. On the contrary, the initial discharge capacities of RF-2-A-60S and RF-2-A-70S electrodes are 876.4 and 772.5 mAh g^{-1} with initial Coulombic efficiencies of 94.9% and 93.3%,

respectively. Meantime, the lithium storage capacity decrease to 427.9 and 416.7 mAh g⁻¹ after 100 cycles with capacity retention of 48.8% and 53.9%, respectively. Apparently RF-1-A-50S and RF-2-A-60S electrodes exhibit better electrochemical activity and higher sulfur utilization relative to their respective high sulfur loading in RF-1-A-60S and RF-2-A-70S electrodes, suggesting excess sulfur not only reduce the conductivity of mesoporous carbon materials but also leads to more severe shuttle effect. In addition, more polysulfides dissolve and diffuse into dead corners, causing the loss of the active material. With its larger pore volume and higher specific surface area, RF-2-A achieves higher discharge capacities. However, the best capacity retention is obtained by RF-1-A, indicating cage-type pores more suitable for the adsorption of polysulfides than long-range-ordered channels. What's more, the discharge voltage plateau of all electrodes around 2.00 V keep highly constant throughout the cycling, proving the high reversibility of cathode electrochemical reaction. It is worth reminding that there are no obvious overcharge of four electrodes during the charge process, demonstrating porous structure of the two carbon can effectively inhibit the shuttle effect with LiNO₃ as an additive in the electrolyte.

The cyclic performances along with the Coulombic efficiencies for the four kinds of C/S cathodes are compared at 0.1 C and 0.2 C. From Fig. 13a, 13b, the initial discharge capacity of 359.6 and 594 mAh g⁻¹ are achieved for RF-1-A-50S and RF-1-A-60S electrodes at 0.2 C, which reach maximum values of 586.6 and 621.7 mAh g⁻¹ on the ninth and seventh cycles, respectively. Capacity stabilize at 528.3 and 408.5 mAh g⁻¹ with the retention of 90.0% and 65.7% after 100 cycles. Since sulfur need to undergone a process of redistribution on the electrode surface, the capacity increase gradually after activation and stabilization. By contrast, RF-2-A-60S and RF-2-A-70S electrodes appear this situation, which are attributed to the fact that the columnar channel structure is more conducive to electron and ion transfer. The cells exhibit initial discharge capacity of 765 and 819.7 mAh g⁻¹ with reversible capacity of 448.5 and 505.5 mAh g⁻¹ corresponding to the retention of 58.6% and 61.5% after 100 cycles, respectively. Under the same sulfur loading density, the thickness of the electrode is proportional to the sulfur content of the carbon material. Hence, the polysulfides formed in the beginning cannot diffuse out of RF-1-A-50S and RF-2-A-60S electrodes in time and prematurely reduce to short-chain and insoluble polysulfides that deposit on the surfaces of carbon, which reducing the utilization of sulfur. Furthermore, dissolved polysulfides form a concentration gradient at the electrode surface to promote the reactions of the non-conductive sulfur and polysulfides species and make it occur on the electrolyte-carbon interface. For RF-1-A-60S and RF-2-A-70S electrodes, the excess surface-deposited sulfur react more quickly and dissolve into the electrolyte to form polysulfides concentration gradient earlier, facilitating subsequent reactions. On account of the strong adsorption of mesoporous carbon, and the common ion effect of polysulfides, less and less polysulfides dissolve into the electrolyte and the specific capacity attenuation is suppressed during subsequent cycles. Consequently, many researchers promote the utilization of sulfur and improve the specific capacity by adding small amount of polysulfides solution into the electrolyte in advance. Meanwhile this part of the polysulfides can passivate the Li surface to inhibit shuttle effect. The kinetics of Li₂S₂/Li₂S is slow. Under the current density of 0.2 C, the cell reactions are faster and the final insoluble products Li₂S₂/Li₂S relatively generate less, so the loss of active material is less. These are the reasons why all four electrodes have better performance at high current densities. Among the four cells, the Coulombic efficiency are up to 99.5% throughout, reflecting that polysulfides are successfully captured within the carbon host.

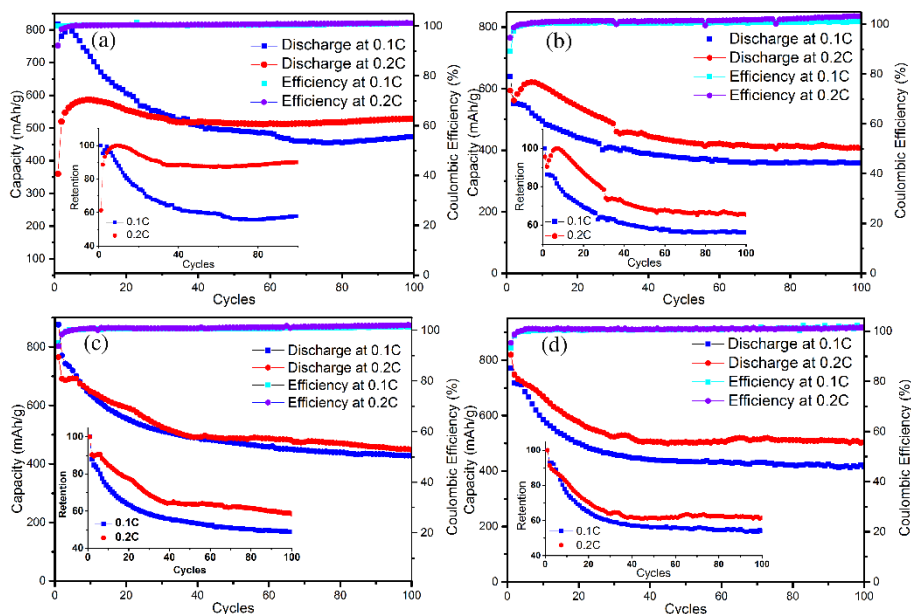


Figure 13. Comparison of the cyclic performances and Coulombic efficiencies of (a) RF-1-A-50S, (b) RF-1-A-60S, (c) RF-2-A-60S and (d) RF-2-A-70S electrodes (inset : retention) under the current density of 0.1 C and 0.2 C.

As we know, the kinetics and cycle stability of the electrode are mainly associated with the conductivity of the whole electrode. Therefore, electrochemical impedance measurements at open circuit voltage and the fully charged state after 100 cycles were recorded to further understand the electrochemical performance of four electrodes at 0.1 C and 0.2 C, as shown in Fig. 14. For all four electrodes, only one depressed semicircle is detected in the Nyquist plot at open circuit voltage, corresponding to the charge-transfer resistance (R_{ct}) and interface resistance (R_0) [44]. The numerical results are illustrated in Table 3. Apparently, due to the porous structure and the high specific surface area of the RF-1-A and RF-2-A, self-discharge of the cells are suppressed. Besides, R_{ct} and R_0 upon the four electrodes are all quite low, proving that highly ordered mesoporous carbon hosts can significantly improve the conductivity of sulfur electrodes. A sloping line is observed in the low-frequency region, which is related to the diffusion and migration of ions. However, it can be found two semicircles existing in all impedance plots at fully charged state after 100 cycles. They can be assigned to the charge-transfer process (R_{ct}) and the resistance from SEI film (R_{SEI}). The late one can mainly be attributed to the formation of insoluble polysulfide species on the electrode surface without being completely reduced during the charging process. The charge-transfer resistance of RF-1-A-50S and RF-1-A-60S composites increases sharply after cycling because the pore size, surface area and pore volume of RF-1-A are smaller than that of RF-2-A, which easily leads to partial aggregations of sulfur and even deposits on the electrode surface. Moreover, R_s of the RF-1-A-50S and RF-1-A-60S electrodes are less than that of RF-2-A-60S and RF-2-A-70S electrodes after cycling, implying the small pore size of RF-1-A has a stronger adsorption capacity for polysulfides. The electrodes show smaller R_{ct} and R_{SEI} values at 0.2 C compared to 0.1 C, which is consistent with the cycle performance.

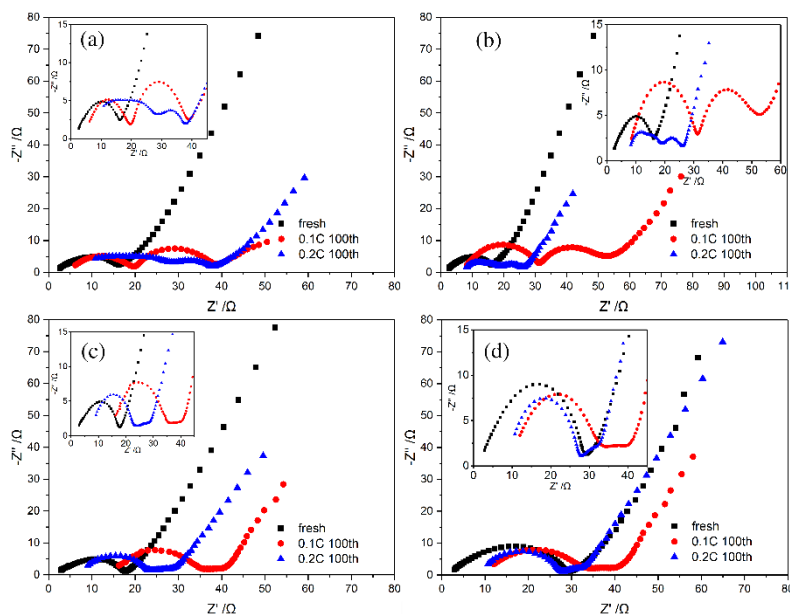


Figure 14. Electrochemical impedance spectra of (a) RF-1-A-50S, (b) RF-1-A-60S, (c) RF-2-A-60S and (d) RF-2-A-70S electrodes recorded from 100 mHz to 100 KHz (before and after 100 cycles the fully charged states under the current density of 0.1 C and 0.2 C).

Table 3. Comparison of R_0 , R_{ct} , and R_{SEI}

| Sample | fresh | | 0.1C 100th | | | 0.2C 100th | | |
|------------|-------|----------|------------|-------|----------|------------|-------|----------|
| | R_0 | R_{ct} | R_0 | R_s | R_{ct} | R_0 | R_s | R_{ct} |
| RF-1-A-50S | 2.61 | 13.53 | 6.20 | 13.43 | 32.97 | 10.86 | 17.9 | 27.64 |
| RF-1-A-60S | 2.61 | 13.54 | 8.40 | 22.86 | 44.8 | 8.22 | 10.92 | 17.98 |
| RF-2-A-60S | 2.91 | 14.78 | 16.28 | 19.88 | 25.7 | 9.11 | 14.9 | 19.88 |
| RF-2-A-70S | 2.96 | 26.29 | 12.09 | 22.29 | 26.88 | 10.75 | 17.33 | 22.32 |

The above results are evidence of highly ordered mesoporous carbon materials RF-1, RF-2 can effectively anchor polysulfides and improve cycle performance. Nonetheless, polysulfides generation is unavoidable for lithium-sulfur batteries during the discharge process. The poor physical adsorption between carbon materials and polysulfides merely delays the mass transfer process of polysulfides, and the “shuttle effect” will continue to appear with the increase of the number of cycles, eventually leading to the loss of active material and the continuous attenuation of capacity. From another perspective, the Li/S battery configuration eventually becomes a liquid electrochemical cell. Hence, chemical adsorption and controlling their kinetics is the key to improving properties.

3.2 Results and Discussion of RF-1-Pt-A and RF-2-Pt-A

3.2.1 Morphology and Structure Characterization

It is well known that the hydrophilic nature of electrocatalyst Pt has been widely used to improve the electrochemical hydrogen insertion into porous carbon materials [29]. Thereby, electrocatalyst Pt tend to form in situ chemisorption with polar natured polysulfides. Simultaneously, the doping of

electrocatalyst Pt can increase the defects of the carbon material and generate more active sites, which is helpful to enhance the conductivity of carbon materials. More notably, use of electrocatalytic Pt electrodes has been shown to improve reaction kinetics of non-aqueous polysulfides [45]. However, it is still a challenge to find simple synthesis of metal catalysts Pt along with high dispersion. Previously reported synthesis methods often required chemical functionalization of carbon materials [46]. In this way, it is ensured that the precursor H_2PtCl_6 is in close contact with the surface of the carbon material and then is reduced to metal catalysts. Here we directly disperse precursor H_2PtCl_6 into the original powder (as-synthesized polymer product RF-1-as, RF-2-as), and then perform a one-step pyrolysis under H_2/Ar (5%/95%) atmosphere to obtain product RF-1-Pt and RF-2-Pt, which were treated by well-established KOH chemical activation to obtain higher surface area and pore volume carbon materials RF-1-Pt-A, RF-2-Pt-A. Similarly, two different sulfur loading for RF-1-Pt-A, RF-2-Pt-A based on the volume of sulfur and end product Li_2S (Table 4) were designed.

Table 4. Theoretical calculation of sulfur content

| | Sulfur | Li_2S |
|------------------------|--------|-----------------------|
| RF-1-A-50S, RF-1-A-60S | 58.2% | 43.5% |
| RF-2-A-60S, RF-2-A-70S | 67.5% | 53.4% |

$$m_s = V_t \times m_c \times \rho \times \frac{32}{46}$$

m_s : quality of sulfur, V_t : pore volume of carbon material, $\text{cm}^3 \text{g}^{-1}$, ρ : $1.66 \text{ g cm}^{-3}(\text{Li}_2\text{S})$, m_c : quality of carbon material.

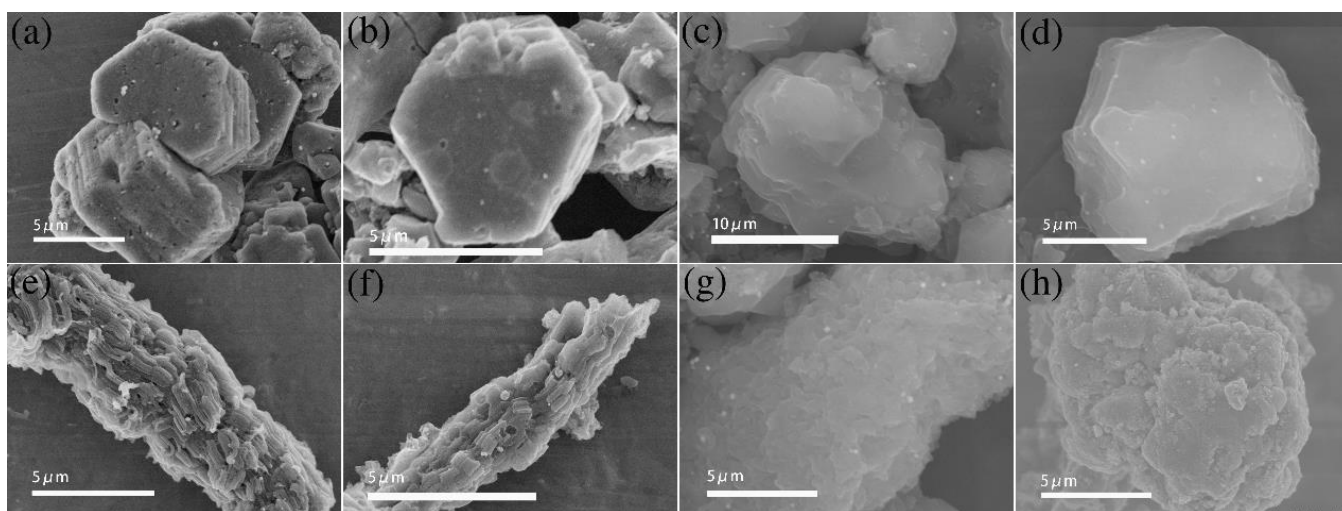


Figure 15. SEM images of (a) RF-1-Pt, (b) RF-1-Pt-A, (c) RF-1-Pt-A-50S, (d) RF-1-Pt-A-60S, (e) RF-2-Pt, (f) RF-2-Pt-A, (g) RF-2-Pt-A-60S and (h) RF-2-Pt-A-70S.

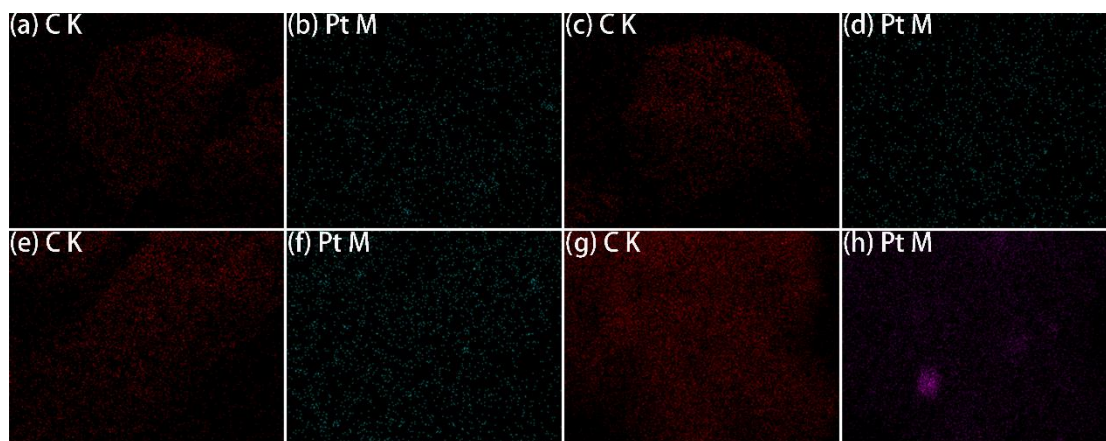


Figure 16. Elemental mapping of C and Pt nanoparticles: (a, b) RF-1-Pt-A-50S, (c, d) RF-1-Pt-A-60S, (e, f) RF-2-Pt-A-60S and (g, h) RF-2-Pt-A-70S.

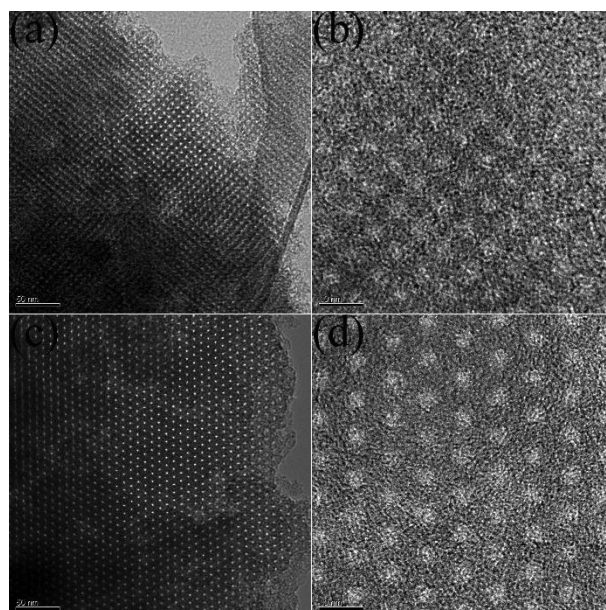


Figure 17. TEM images of (a, b) RF-1-Pt-A, (c) RF-2-Pt-A.

In case of RF-1-Pt and RF-2-Pt, irregularly polyhedral particles with growth patterns and rod-like domains aggregating along the long axis were observed to be similar to RF-1 and RF-2 (Fig. 2a, 2e), as shown in Fig. 15. This suggests that the deposited Pt didn't destroy the carbon meso-structure. The bright spots on surface of RF-1-Pt and RF-2-Pt can be attributed to the metallic Pt nanoparticles. Apart from the rough morphology of RF-1-Pt-A and RF-2-Pt-A, the structure did not change. Further, EDS images of four C/S composites illustrated in Fig. 16a-h are evident that Pt nanoparticles maintained a high degree of dispersion in the carbon matrix. Both TEM images (Fig. 17) of RF-1-Pt-A and RF-2-Pt-A show large-area ordered regions, demonstrating the ordered cubic $Im\bar{3}m$ mesostructure and a high-quality hexagonal mesostructure, respectively, which is similar to the RF-1-A and RF-2-A. There are no aggregations of sulfur powder on the surface of RF-1-Pt-A-50S and RF-1-Pt-A-60S, while bright spots are attributed to metallic Pt can still be seen, which indicates that the elemental sulfur penetrated into the

pore structure of the RF-1-Pt-A. The surface of RF-2-Pt-A-60S and RF-2-Pt-A-70S form a clear contrast. In particular, the surface of RF-2-Pt-A-70S is covered with a large amount of sulfur. The diffraction peaks ascribed to Fddd orthorhombic structure reflections of pure sulfur are exist in XRD patterns of RF-2-Pt-A-60S and RF-2-Pt-A-70S, as shown in Fig. 18. As for the XRD patterns of RF-1-Pt-A-50S and RF-1-Pt-A-60S, except the intrinsic peaks of RF-1-Pt-A, no crystal diffraction peaks indexed to sulfur were found.

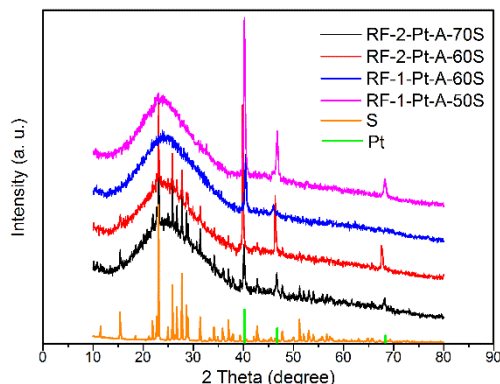


Figure 18. XRD patterns of pure S, RF-1-Pt-A-50S, RF-1-Pt-A-60S, RF-2-Pt-A-60S and RF-2-Pt-A-70S.

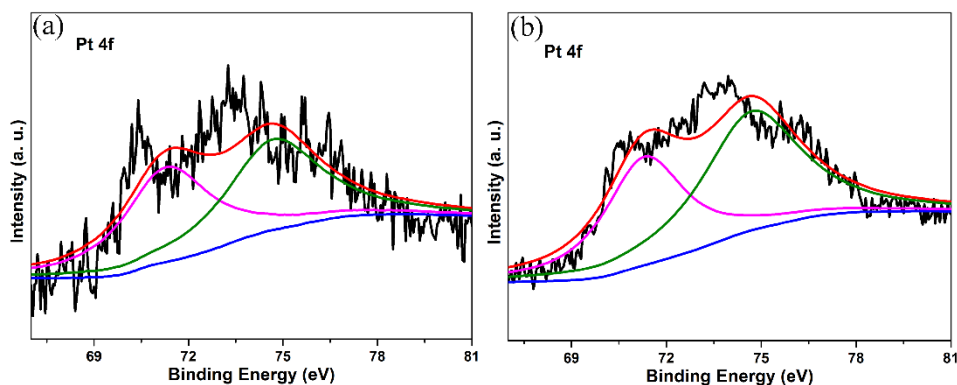


Figure 19. XP spectra of Pt 4f regions of (a) RF-1-Pt-A and (b) RF-2-Pt-A.

Table 5. Structural parameters of carbon samples

| Sample | $S_{\text{BET}}^{\text{a}}$ ($\text{m}^2 \text{g}^{-1}$) | V_{t}^{b} ($\text{cm}^3 \text{g}^{-1}$) | S_{mi}^{c} ($\text{m}^2 \text{g}^{-1}$) | V_{mi}^{d} ($\text{cm}^3 \text{g}^{-1}$) |
|-----------|---|--|--|---|
| RF-1-A-Pt | 1758 | 1.13 | 1163 | 0.52 |
| RF-2-A-Pt | 1532 | 1.03 | 986 | 0.445 |
| RF-1-Pt | 660 | 0.50 | 359 | 0.16 |
| RF-2-Pt | 666 | 0.52 | 355 | 0.16 |

^a S_{BET} : BET specific surface area; ^b V_{t} : total volume; ^c S_{mi} : micropore surface area, was calculated from t -plot method; ^d V_{mi} : micropore volume, was calculated from t -plot method.

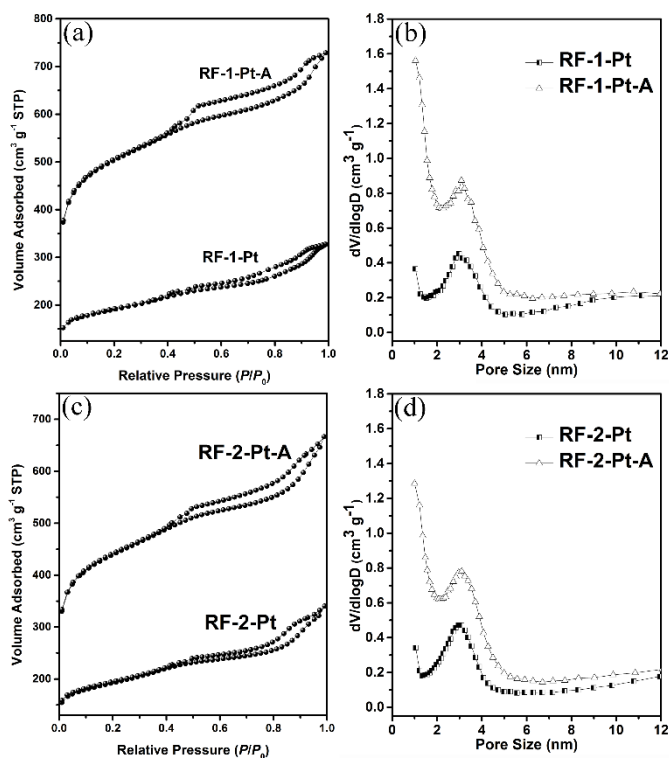


Figure 20. Nitrogen sorption isotherms and PSD curves of different carbon hosts: (a) RF-1-Pt, (b) RF-1-Pt-A, (c) RF-2-Pt and (b) RF-2-Pt-A.

This result is in line with the theoretical calculation of the sulfur content. Moreover, there are determined that the diffraction peaks at $2\theta=40.2^\circ$, 46.8° , and 68.3° are assigned to metal Pt among the four XRD patterns. Fig. 19 shows that the Pt 4f doublet with binding energy of Pt 4f_{7/2} and Pt 4f_{5/2} peaks at about 71.3 eV and 74.7 eV after the reduction, respectively, which further proves the formation of metallic Pt from Pt ions.

Surface area and pore volume of Pt decorated mesoporous carbon materials calculated from nitrogen sorption isotherms depicted in Fig. 20 are presented Table 5. As observed, RF-1-Pt and RF-2-Pt also exhibit Type-IV curve with clear capillary condensation steps at $P/P_0=0.4-0.6$ providing evidence of uniformed meso-pore distributions [47]. After KOH chemical activation, surface area of RF-1-Pt and RF-2-Pt increase from $660 \text{ m}^2 \text{ g}^{-1}$ and $666 \text{ m}^2 \text{ g}^{-1}$ to $1758 \text{ m}^2 \text{ g}^{-1}$ and $1532 \text{ m}^2 \text{ g}^{-1}$, respectively. In the meantime, pore volume has found to be almost doubled. Compared with Table 2, surface area and pore volume of RF-1-Pt-A significantly larger than that of RF-1-A, while pore volume of RF-1-Pt-A is almost unchanged, and surface area is smaller. The PSD curves (Fig. 20c-d) of four samples are relatively narrow. The mesopore diameter of RF-2-Pt and RF-2-Pt-A are about 3.09 nm and 3.1 nm, respectively, which is obviously decline than that of RF-2-A. Based on the previous analysis, we know that changes in the pore volume and surface area have a great influence on the performance of the battery.

Furthermore, the extent of the binding between the carbon and sulfur nanocrystals was identified by XPS spectra in Fig. 21a-k. The C 1s spectrum of RF-1-Pt-A and RF-2-Pt-A are composed of C-C bond (284.5 eV), C=N bond (285.3 eV), C-O bond (286.4 eV), and C=O bond (288.4 eV), respectively. The reduction of the peak intensity of C=O groups demonstrate C=O groups are removed and converted to C-O-S bonds. From Fig. 21d, 21f, 21i, 21k, XPS spectra of deconvoluted S 2p peaks at 163.6 and

164.8 eV ($S\ 2p_{3/2}$), and 164.3 and 165.5 eV ($S\ 2p_{1/2}$), respectively, corresponding to S-S bond and S-O species. This proves that the sulfur nanocrystals are uniformly encapsulated within carbon through S-O bonds [48]. Likewise, there are four different peaks with a binding energy of 398.3 eV, 400.2 eV, 401.1 eV, and 402.9 eV corresponding to pyridinic-N (N-6), pyrrolic-N (N-5), quaternary-N (N-Q) and oxidized pyridine-N (N-X) [49,50] were illustrated in Fig. 22a-f.

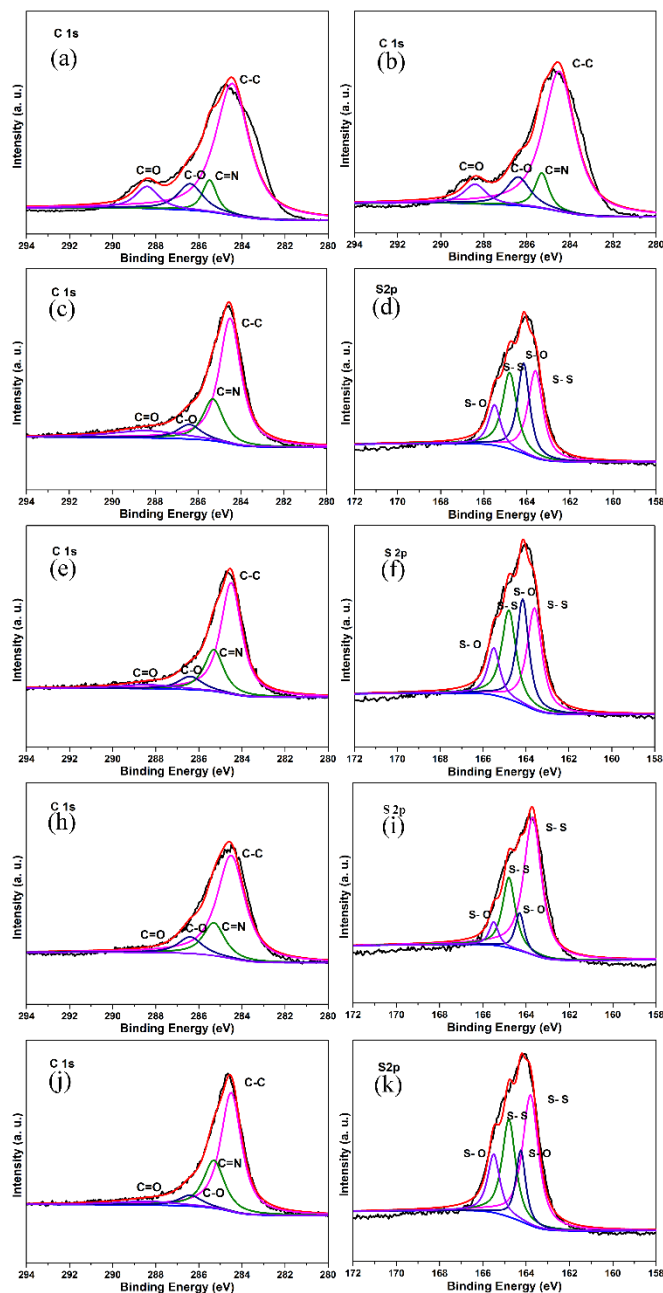


Figure 21. High-resolution C 1s and S 2p spectra of (a) RF-1-Pt-A, (b) RF-2-Pt-A, (c, d) RF-1-Pt-A-50S, (e, f) RF-1-Pt-A-60S, (g, h) RF-2-Pt-A-60S and (i, j) RF-2-Pt-A-70S.

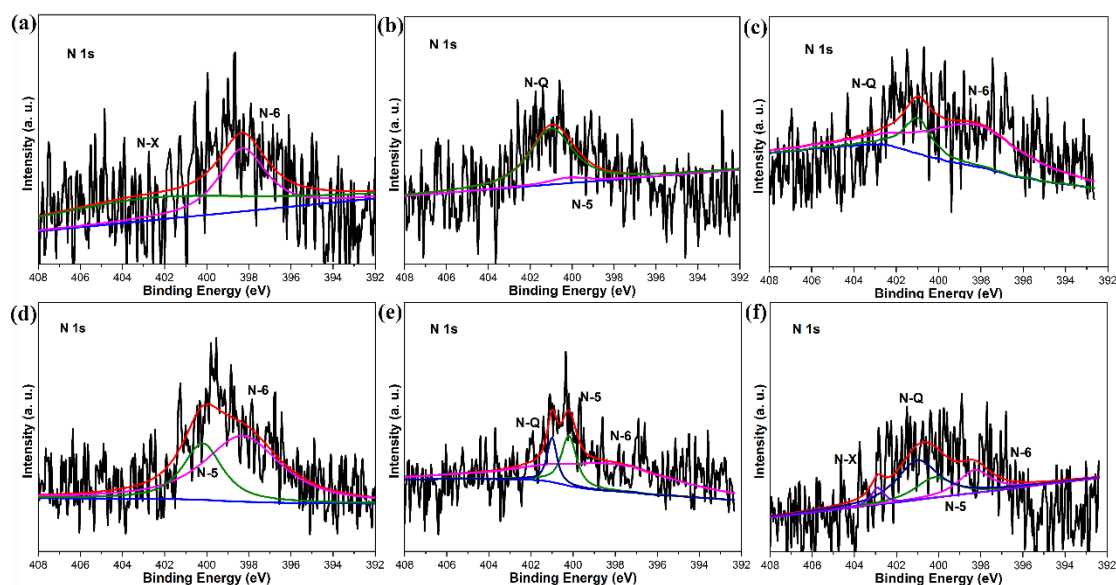


Figure 22. High-resolution N 1s spectra of (a) RF-1-Pt-A, (b) RF-1-Pt-A-50S, (c) RF-1-Pt-A-60S, (d) RF-2-Pt-A, (eh) RF-2-Pt-A-60S and (f) RF-2-Pt-A-70S.

3.2.2 Electrochemical Performance

To evaluate the electrochemical performance of four kinds of C/S cathodes, galvanostatic charge/discharge studies were carried out at a constant current rate of 0.2 C, and obtained results for 100 cycles were illustrated in Fig. 23a-d. Considering the activation of the surface electrochemical activity by the charge–discharge process, all cells are first cycled at 0.1 C for three cycles. It was observed that electrodes display two distinguishable discharge plateaus similar to Fig. 12. The RF-1-Pt-A-50S and RF-1-P-A-60S electrodes exhibit a high initial specific capacity of 1105 and 811 mAh g⁻¹, respectively, which is increased capacity by 26% and 21% over RF-1-A-50S and RF-1-A-60S. Apparently, the increase in surface area and pore volume results in better infiltration of the electrolyte and higher utilization of the active material at the same time. To our surprise, the RF-2-Pt-A-60S and RF-2-A-Pt-70S electrodes still deliver about 855.2 and 794 mAh g⁻¹ of initial discharge capacities without affecting by reduction of surface area. When tested at a rate of 0.2 C, the RF-1-Pt-A-50S and RF-1-A-Pt-60S electrodes carry initial discharge capacities of 834.5 and 715.2 mAh g⁻¹, and achieve 59.7% and 74.3% of the discharge capacity retention after 100 cycles, respectively. The initial discharge capacities of RF-2-Pt-A-60S and RF-2-A-Pt-70S electrodes are 650.4 and 732.5 mAh g⁻¹, and stabilized at 399.5 and 495 mAh g⁻¹ with the retention of 61.4% and 67.9% after 100 cycles. It is apparent that the sulfur utilization and cyclic stability of RF-1-Pt-A and RF-2-Pt-A are higher than that of RF-1-A and RF-2-A. Fig. 24 compare the cycling performances and Coulombic efficiencies of four samples. As we know, the surface area of carbon has two functions. On one hand, the larger the surface area, the more dilute the dispersion of sulfur will be with the same sulfur content in the composite. On the other hand, during the electrochemical process, higher surface area translates to decreased real current density on carbon substrates [51-53]. As a result, the RF-1-Pt-A-50S and RF-1-A-Pt-60S electrodes are more conducive to electrolyte infiltration, and obtain higher initial discharge capacity. However, in the case of a decreased

surface area, RF-2-Pt-A-60S and RF-2-A-Pt-70S electrodes achieve better performance, which reflect Pt nanoparticle affords the adsorption of polysulfides through strong chemical interaction during the discharge process and promote their conversion to soluble long-chain polysulfides and elemental sulfur during the charging process.

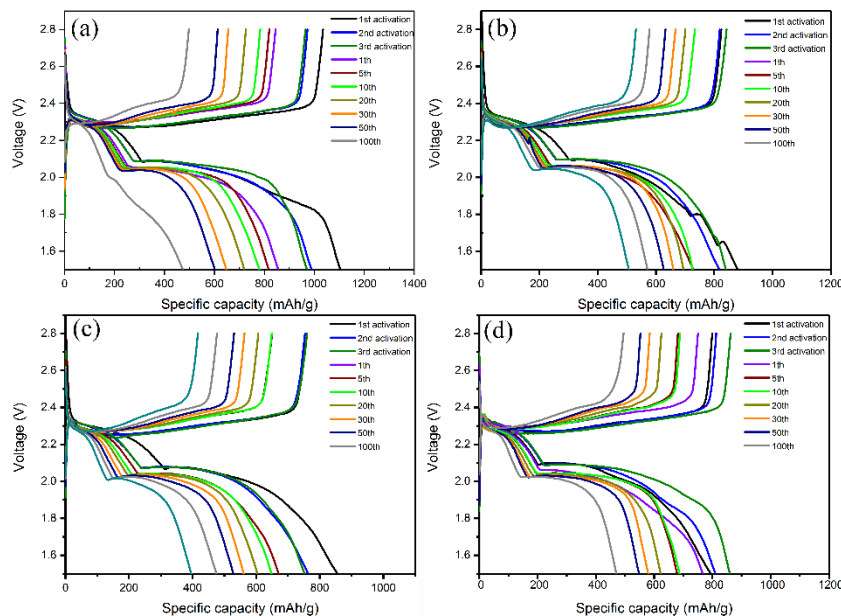


Figure 23. Charge/discharge profiles of (a) RF-1-Pt-A-50S, (b) RF-1-Pt-A-60S, (c) RF-2-Pt-A-60S and (d) RF-2-Pt-A-70S electrodes under the current density of 0.2 C in a voltage of 1.5-2.8 V.

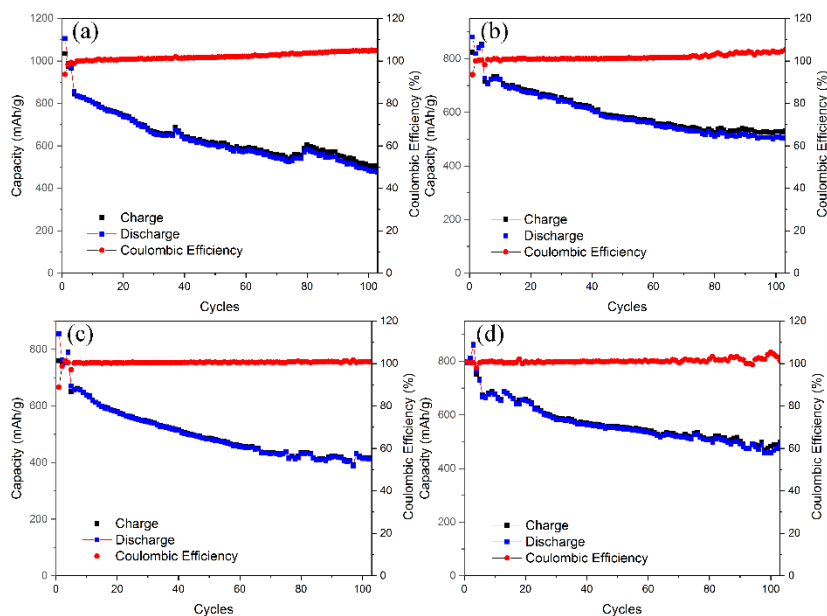


Figure 24. The cyclic performances and Coulombic efficiencies of (a) RF-1-Pt-A-50S, (b) RF-1-Pt-A-60S, (c) RF-2-Pt-A-60S and (d) RF-2-Pt-A-70S electrodes.

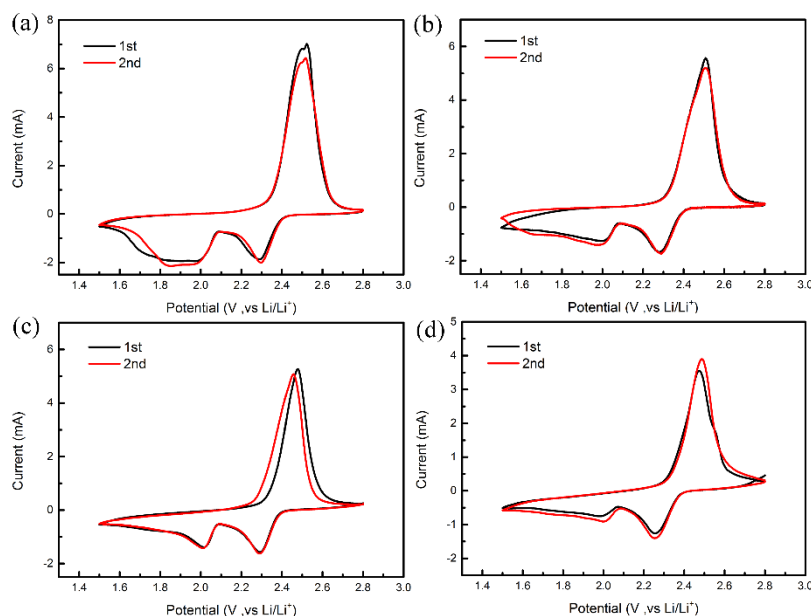


Figure 25. Cycle voltammetry of (a) RF-1-Pt-A-50S, (b) RF-1-Pt-A-60S, (c) RF-2-Pt-A-60S and (d) RF-2-Pt-A-70S electrodes.

Table 6. electrocatalytic parameters for different electrodes are derived from cyclic voltammograms and potentiostatic polarization

| Sample | Reduction peak potential (V) | | Oxide peak potential (V) | Peak separation(V) |
|---------------|------------------------------|-------|--------------------------|--------------------|
| RF-1-A-50S | 2.31 | 1.987 | 2.504 | 0.517 |
| RF-1-A-60S | 2.274 | 2.009 | 2.492 | 0.483 |
| RF-2-A-60S | 2.277 | 2.01 | 2.515 | 0.505 |
| RF-2-A-70S | 2.276 | 1.999 | 2.535 | 0.536 |
| RF-1-A-Pt-50S | 2.291 | 1.981 | 2.498 | 0.517 |
| RF-1-A-Pt-60S | 2.287 | 2.003 | 2.510 | 0.507 |
| RF-2-A-Pt-60S | 2.292 | 2.016 | 2.477 | 0.461 |
| RF-2-A-Pt-70S | 2.256 | 1.980 | 2.474 | 0.494 |

Additionally, Pt as an electrocatalyst can help to convert polysulfide deposits back to soluble long-chain polysulfide and hence enhance reaction kinetics and retain high Coulombic efficiency [54-57]. The deposition of insulating Li_2S_2 and Li_2S on the surface of the cathode not only block the pores, but also results in an increase of internal resistance. It is well known that Pt has a particularly high conductivity, which may help to decrease the resistance of electron conduction and transfer [58,59]. Thus, electrocatalyst Pt is promising to enhance reaction kinetics and decrease cell polarization. Among the four cells, the Coulombic efficiencies are all above 99.5% throughout, indicating Pt is beneficial for the restriction of the shuttle effect and the overall stability and activity of electrocatalyst towards long cycling performance.

To further understanding electrocatalytic behavior of Pt, cyclic voltammograms were recorded on all four electrodes and resulting curves were depicted in Fig. 25. Similar to Fig. 11, two characteristic reduction peaks and an oxidation peak were observed. On careful observation, peak potential along with potentiostatic polarization are quantified and summarized in Table 6. As anticipated, the distinguishable

negative shift in oxidation peak and decrease in potentiostatic polarization are evidence of the superior catalytic activity of Pt toward the polysulfides conversion process. The distinguishable positive shift in the reduction peaks and negative shift in the oxidation peaks of the cathode indicate the improved polysulfide redox kinetics by Pt. It is apparent that these peaks shifting indicate an increase in cell reaction kinetics and a decrease in cell polarization, which is helpful to obtain high capacity utilization of sulfur and long cycling performance [60,61].

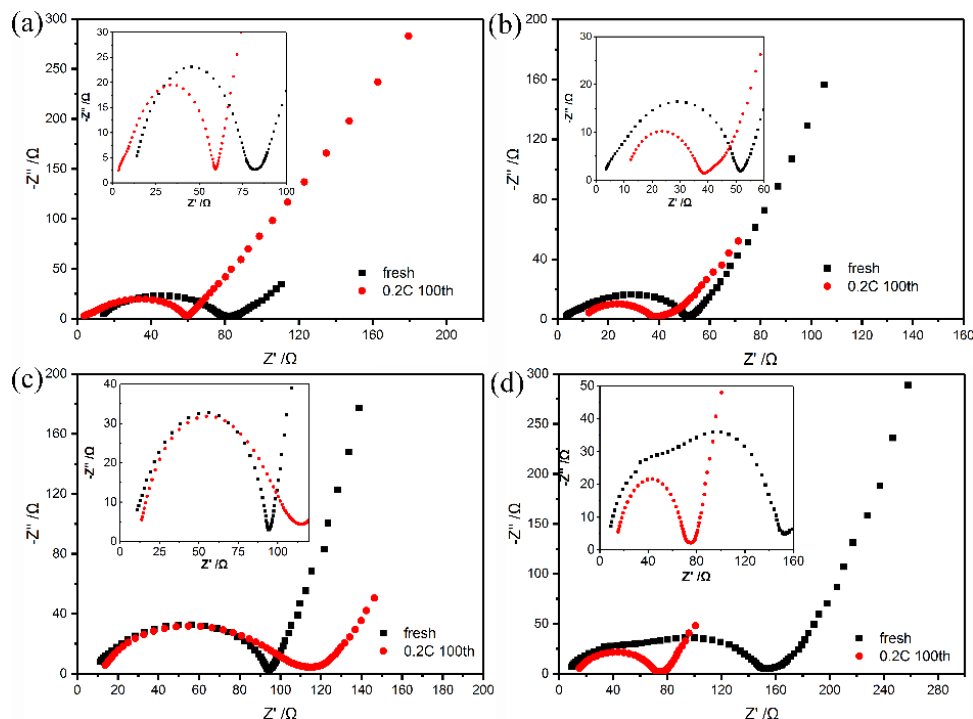


Figure 26. Electrochemical impedance spectra of (a) RF-1-Pt-A-50S, (b) RF-1-Pt-A-60S, (c) RF-2-Pt-A-60S and (d) RF-2-Pt-A-70S electrodes recorded from 100 mHz to 100 KHz (before and after 100 cycles the fully charged states under the current density of 0.2 C).

Further evidence of effect of catalyst was excavated by the impedance measurements. From Fig. 26, the Nyquist plots for all four fresh cells are composed of a depressed semicircle in the high-to-medium frequency region and a sloping line in the low-frequency region. Insoluble $\text{Li}_2\text{S}_2/\text{Li}_2\text{S}$ on the electrode surface without being completely reduced during the charging process give rise to a decrease in charge-transfer resistance. However, all impedance plots at fully charged states show only one depressed semicircle instead of two semicircles in the high-to-medium frequency region after 100 cycles contrast with Fig. 14. Hence, the presence of catalyst of Pt plays a crucial role in converting $\text{Li}_2\text{S}_2/\text{Li}_2\text{S}$ into dissolvable polysulfides and elemental sulfur during the charging process. Besides, the R_{ct} immensely decrease after cycles, which is attributed to Pt facilitates relocation of the migrated active materials to the electrochemically favorable position. In summary, a higher affinity between Pt and soluble polysulfides and converting them into long-chain species is important for high capacity utilization of Sulfur and long cycle life.

4. CONCLUSION

In summary, highly ordered *Resorcinol-Formaldehyde* (RF) resin based mesoporous carbon materials were applied in the cathode material of lithium sulfur battery. The micro-mesoporous hierarchial carbon with large pore volume and high specific surface with hexagonal and cubic structures were obtained through KOH activation process. When the sulfur content was 2 mg cm⁻², the sulfur/carbon composite electrode exhibited the best cycling performance when the electrolyte/sulfur ratio E/S was 15 μ L mg⁻¹. Due to the advantages of pore volume and specific surface area, the sulfur loading within RF-2-A carbon with hexagonal mesostructure is up to 70%. The first discharge capacity at 0.2 C current density is 819.7 mAh g⁻¹. After 100 cycles, the reversible capacity is 504.5 mAh g⁻¹, the capacity retention rate is 61.5%, and the Coulombic efficiency is close to 100%. In addition, the cage-type pores with the small pore entrance in RF-1-A are more beneficial to the adsorption of polysulfide than the long range column holes in RF-2-A, which can inhibit the shuttle effect, achieve better cyclic stability, and improve the battery performance. However, the weak physical adsorption of polysulfide with mesoporous carbon can only delay the mass transfer process of polysulfide, and the capacity decay is still constant. In this study, the electrocatalytic properties of metal Pt were taken into account, and metal Pt nanoparticles were obtained by the reduction of metal directly in the process of carbonization of the raw powder. The capacity retention of RF-1-Pt-A-60S and RF-2-A-Pt-70S composites is 74.3% and 67.9% respectively after 100 cycles of 0.2 C current density. With the doping of metallic Pt onto carbon host, the composited carbon material can in situ adsorb long chain polysulfide, prevent the free diffusion and migration of polysulfides, inhibit the shuttle effect, and catalyze the conversion of short chain polysulfide to long chain polysulfide, reduce the deposition of Li₂S₂ and Li₂S, decrease the battery impedance, improve the utilization of active substances, and maintain the cyclic stability.

ACKNOWLEDGEMENTS

This work was partially supported by the National Nature Science Foundation of China (11474226, 51676143 and 21476177), Fundamental Research Funds for the Central Universities. (WUT: 2017-IB-003; 2018-IB-022 and 2018-IB-028) and Foshan Innovative and Entrepreneurial Research Team Program (2014IT100062). The authors thank Dr. Xiao-Qing Liu for his assistance conducting TEM.

References

1. Y. J. Liu, P. He and H. S. Zhou, *Adv. Energy Mater.*, 8 (2018) 170160.
2. R. P. Fang, S. Y. Zhao, Z. H. Sun, W. Wang, H. M. Cheng and F. Li, *Adv. Mater.*, 29 (2017) 1602863.
3. X. Liu, J. Q. Huang, Q. Zhang and L. Q. Mai, *Adv. Mater.*, 29 (2017) 1601759.
4. K. Fu, Y. H. Gong, G. T. Hitz, D. W. McOwen, Y. J. Li, S. M. Xu, Y. Wen, L. Zhang, C. W. Wang, G. Pastel, J. Q. Dai, B. Y. Liu, H. Xie, Y. G. Yao, E. D. Wachsman and L. B. Hu, *Energy Environ. Sci.*, 10 (2017) 1568.
5. H. J. Peng, J. Q. Huang, X. B. Cheng and Q. Zhang, *Adv. Energy Mater.*, 7 (2017) 1700260.
6. Y. Zhong, X. H. Xia, S. J. Deng, J. Y. Zhan, R. Y. Fang, Y. Xia, X. L. Wang, Q. Zhang and J. P. Tu, *Adv. Energy Mater.*, 8 (2018) 1701110.
7. K. Mi, Y. Jiang, J. K. Feng, Y. T. Qian and S. L. Xiong, *Adv. Funct. Mater.*, 26 (2016) 1571.

8. S. Q. Chen, B. Sun, X. Q. Xie, A. K. Mondal, X. D. Huang and G. X. Wang, *Nano Energy*, 16 (2015) 268.
9. M. K. Rybarczyk, H. J. Peng, C. Tang, M. Lieder, Q. Zhang and M. M. Titirici, *Green Chem.*, 18 (2016) 5169.
10. Z. H. Chen, X. L. Du, J. B. He, F. Li, Y. Wang, Y. L. Li, B. Li and S. Xin, *ACS Appl. Mater. Interfaces*, 9 (2017) 33855.
11. J. H. Zheng, G. N. Guo, H. W. Li, L. Wang, B. W. Wang, H. J. Yu, Y. C. Yan, D. Yang and A. G. Dong, *ACS Energy Lett.*, 2 (2017) 1105.
12. H. Y. Shao, F. Ai, W. K. Wang, H. Zhang, A. B. Wang, W. Feng and Y. Q. Huang, *J. Mater. Chem. A*, 5 (2017) 19892.
13. T. Zhao, Y. Ye, X. Peng, G. Divitini, H. K. Kim, C. Y. Lao, P. R. Coxon, K. Xi, Y. J. Liu, C. Ducati, R. J. Chen and R. V. Kumar, *Adv. Funct. Mater.*, 26 (2016) 8418.
14. D. Liu, H. U. Yan-Yan, C. Zeng and D.-Y. Qu, *Acta Phys.-Chim. Sin.*, 32 (2016) 2826.
15. S. H. Liu, J. Li, X. Yan, Q. F. Su, Y. H. Lu, J. S. Qiu, Z. Y. Wang, X. D. Lin, J. L. Huang, R. L. Liu, B. N. Zheng, L. Y. Chen, R. W. Fu and D. C. Wu, *Adv. Mater.*, 30 (2018) 1706895.
16. D. H. Liu, C. Zhang, G. M. Zhou, W. Lv, G. W. Ling, L. J. Zhi and Q. H. Yang, *Adv. Sci.*, 5 (2018) 1700270.
17. D. Liu, J.-H. Lei, L.-P. Guo, D. Qu, Y. Li and B.-L. Su, *Carbon*, 50 (2012) 476.
18. D. Zhao, Q. Huo, J. Feng, B. F. Chmelka and G. D. Stucky, *J. Am. Chem. Soc.*, 136 (2014) 10546.
19. H. S. Ryu, H. J. Ahn, K. W. Kim, J. H. Ahn and J. Y. Lee, *J. Power Sources*, 153 (2006) 360.
20. C. Lai, X. P. Gao, B. Zhang, T. Y. Yan and Z. Zhou, *J. Phys. Chem. C*, 113 (2009) 4712.
21. X. Ji, K. T. Lee and L. F. Nazar, *Nat. Mater.*, 8 (2009) 500.
22. C. Liang, N. J. Dudney and J. Y. Howe, *Chem. Mater.*, 21 (2009) 4724.
23. N. Jayaprakash, J. Shen, S. S. Moganty, A. Corona and L. A. Archer, *Angew. Chem.-Int. Edit.*, 50 (2011) 5904.
24. X. Li, Y. Cao, W. Qi, L. V. Saraf, J. Xiao, Z. Nie, J. Mietek, J.-G. Zhang, B. Schwenzer and J. Liu, *J. Mater. Chem.*, 21 (2011) 16603.
25. X. Liang, Z. Wen, Y. Liu, M. Wu, J. Jin, H. Zhang and X. Wu, *J. Power Sources*, 196 (2011) 9839.
26. J. R. Matos, M. Kruk, L. P. Mercuri, M. Jaroniec, L. Zhao, T. Kamiyama, O. Terasaki, T. J. Pinnavaia and Y. Liu, *J. Am. Chem. Soc.*, 125 (2003) 821.
27. L. Ji, M. Rao, H. Zheng, L. Zhang, Y. Li, W. Duan, J. Guo, E. J. Cairns and Y. Zhang, *J. Am. Chem. Soc.*, 133 (2011) 18522.
28. C.-Y. Fan, P. Xiao, H.-H. Li, H.-F. Wang, L.-L. Zhang, H.-Z. Sun, X.-L. Wu, H.-M. Xie and J.-P. Zhang, *ACS Appl. Mater. Interfaces*, 7 (2015) 27959.
29. H. Al Salem, G. Babu, C. V. Rao and L. M. R. Arava, *J. Am. Chem. Soc.*, 137 (2015) 11542.
30. D. Liu, Y. Li, D. Zheng, G. Wang, D. Qu, Z.-z. Xie, C. Li, J. Lei and D. Qu, *Chemistryselect*, 2 (2017) 7160.
31. D. Liu, G. Cheng, H. Zhao, C. Zeng, D. Qu, L. Xiao, H. Tang, Z. Deng, Y. Li and B.-L. Su, *Nano Energy*, 22 (2016) 255.
32. J. Zheng, D. Lv, M. Gu, C. Wang, J.-G. Zhang, J. Liu and J. Xiao, *J. Electrochem. Soc.*, 160 (2013) A2288.
33. X. N. Li, J. W. Liang, Y. Lu, Z. Hou, Q. S. Cheng, Y. C. Zhu and Y. T. Qian, *Angew. Chem.-Int. Edit.*, 56 (2017) 2937.
34. J. Cai, C. Wu, Y. Zhu, K. Zhang and P. K. Shen, *J. Power Sources*, 341 (2017) 165.
35. X. Gu, C.-j. Tong, C. Lai, J. Qiu, X. Huang, W. Yang, B. Wen, L.-m. Liu, Y. Hou and S. Zhang, *J. Mater. Chem. A*, 3 (2015) 16670.
36. D. Aurbach, E. Pollak, R. Elazari, G. Salitra, C. S. Kelley and J. Affinito, *J. Electrochem. Soc.*, 156 (2009) A694.
37. S. S. Zhang and J. A. Read, *J. Power Sources*, 200 (2012) 77.
38. S. S. Zhang, *Electrochim. Acta*, 70 (2012) 344.

39. S. S. Zhang, *J. Electrochem. Soc.*, 159 (2012) A920.
40. J. Song, Z. Yu, M. L. Gordin and D. Wang, *Nano Lett*, 16 (2016) 864.
41. Y. Li, J. Fang, J. Zhang, J. Yang, R. Yuan, J. Chang, M. Zheng and Q. Dong, *ACS Nano*, 11 (2017) 11417.
42. X.-L. Du, Y. You, Y. Yan, D. Zhang, H.-P. Cong, H. Qin, C. Zhang, F.-F. Cao, K.-C. Jiang, Y. Wang, S. Xin and J.-B. He, *ACS Appl. Mater. Interface*, 8 (2016) 22261.
43. J. Zheng, M. Gu, C. Wang, P. Zuo, P. K. Koech, J.-G. Zhang, J. Liu and J. Xiao, *J. Electrochem. Soc.*, 160 (2013) A1992.
44. D. Qu, X. Zhu, D. Zheng, Y. Zheng, D. Liu, Z. Xie, H. Tang, J. Wen, X. You, L. Xiao, J. Lei and D. Qu, *Electrochim. Acta*, 174 (2015) 400.
45. G. Babu, K. Ababtain, K. Y. S. Ng and L. M. R. Arava, *Sci. Rep.*, 5 (2015) 8763.
46. J. Zheng, M. Gu, M. J. Wagner, K. A. Hays, X. Li, P. Zuo, C. Wang, J.-G. Zhang, J. Liu and J. Xiao, *J. Electrochem. Soc.*, 160 (2013) A1624.
47. F. Xu, Z.W. Tang, S.Q. Huang, L.Y. Chen, Y.R. Liang, W.C. Mai, H. Zhong, R.W. Fu, D.C. Wu, *Nat. Commun.*, 6 (2015) 10.
48. J. Zhang, Y. Shi, Y. Ding, L. Peng, W. Zhang, G. Yu, *Adv. Energy Mater.*, 7 (2017) 1602876.
49. D. Su, M. Cortie, G. Wang, *Adv. Energy Mater.*, 7 (2017) 1602014.
50. M. Chen, Q. Lu, S. Jiang, C. Huang, X. Wang, B. Wu, K. Xiang, Y. Wu, *Chem. Eng. J.*, 335 (2018) 831.
51. C.B. Jin, W.K. Zhang, Z.Z. Zhuang, J.G. Wang, H. Huang, Y.P. Gan, Y. Xia, C. Liang, J. Zhang, X.Y. Tao, *J. Mater. Chem. A*, 5 (2017) 632.
52. D.R. Deng, F. Xue, Y.J. Jia, J.C. Ye, C.D. Bai, M.S. Zheng, Q.F. Dong, *ACS Nano*, 11 (2017) 6031.
53. S.K. Park, J. Lee, T. Hwang, B. Jang, Y. Piao, *ACS Appl. Mater. Interfaces*, 9 (2017) 2430.
54. J. Xu, W. Zhang, H. Fan, F. Cheng, D. Su, G. Wang, *Nano Energy*, 51 (2018) 73.
55. Y.B. Huang, J. Liang, X.S. Wang, R. Cao, *Chem. Soc. Rev.*, 46 (2017) 126.
56. X. Wu, S.S. Yao, J.L. Hou, M.X. Jing, X.Y. Qian, X.Q. Shen, J. Xiang, X.M. Xi, *J. Nanosci. Nanotechnol.*, 17 (2017) 2482.
57. Z.J. Lin, X. Li, W.L. Huang, X. Zhu, Y. Wang, Z.Q. Shan, *ChemElectroChem*, 4 (2017) 2577.
58. J. Pu, Z. Shen, J. Zheng, W. Wu, C. Zhu, Q. Zhou, H. Zhang, F. Pan, *Nano Energy*, 37 (2017) 7.
59. F. Sun, H. Cheng, J. Chen, N. Zheng, Y. Li, J. Shi, *ACS Nano*, 10 (2016) 8289.
60. X. Liu, J.Q. Huang, Q. Zhang, L.Q. Mai, *Adv. Mater.*, 29 (2017) 25.